RESEARCH ARTICLE

Key Points:
- Presents the spatial distribution and temporal variation of radium isotopes in coastal groundwater mixing zone for the first time
- Dynamic of radium isotopes detects the differences of geochemical reactions in upper saline plume and salt wedge
- Dynamic of radium isotopes detects the dissimilarity of hydrodynamics in upper saline plume and salt wedge

Supporting Information:
- Supporting Information S1

Correspondence to:
J. J. Jiao,
jjiao@hku.hk

Using Tidal Fluctuation-Induced Dynamics of Radium Isotopes (^{224}Ra, ^{223}Ra, and ^{228}Ra) to Trace the Hydrodynamics and Geochemical Reactions in a Coastal Groundwater Mixing Zone

Yi Liu[1,2] , Jiu Jimmy Jiao[1,2] , Wenzhao Liang[1,2], and Xin Luo[1,2]

[1]Department of Earth Sciences, The University of Hong Kong, Hong Kong, China, [2]Shenzhen Research Institute, The University of Hong Kong, Shenzhen, China

Abstract The reactive transport of radium isotopes (^{224}Ra, ^{223}Ra, and ^{228}Ra) in coastal groundwater mixing zones (CGMZs) is sensitive to shifts of redox conditions and geochemical reactions induced by tidal fluctuation. This study presents a spatial distribution and temporal variation of radium isotopes in the CGMZ for the first time. Results show that the activity of radium isotopes in the upper saline plume (USP) is comparatively low due to a short residence time and mixing loss induced by the infiltration of low radium seawater whereas the activity of radium isotopes in the salt wedge (SW) is comparatively high due to a long residence time in the aquifer. The spatial distribution of radium isotopes is determined by the partitioning of radium isotopes, groundwater residence time, and relative ingrowth rates of radium isotopes. In addition, the variation of radium isotopes in the USP lags slightly (~0 h) whereas the fluctuation of radium isotopes in the SW lags significantly (~12 h) behind sea level oscillation. Tidal fluctuation affects the partitioning of radium isotopes through controlling seawater infiltration and subsequently influences the dynamics of radium isotopes in the USP. Concurrently, seawater infiltration significantly affects geochemical processes such as the production of nutrients and total alkalinity. Therefore, radium dynamics in the USP have implications for these geochemical processes. The variation of radium isotopes in the USP also has potential implications for transformation of trace metals such as iron and manganese because of the close affinity of radium isotopes to manganese and iron oxides.

1. Introduction

Radium isotopes (^{224}Ra, ^{223}Ra, and ^{228}Ra) are naturally occurring radionuclides with different half-lives (3.66 days, 11.4 days, and 5.75 year for ^{224}Ra, ^{223}Ra, and ^{228}Ra, respectively). As powerful tracers, ^{224}Ra, ^{223}Ra, and ^{228}Ra are widely used to investigate estuarine/ocean mixing, submarine groundwater discharge (SGD), water/soil interaction, and benthic flux (Cai et al., 2014; Hancock et al., 2000; Luo et al., 2014; Moore, 2000a, 2000b, 2008; Moore et al., 2006). When applying radium isotopes as tracers to estimate SGD flux, a large proportion of uncertainty of SGD flux is from uncertainties in selecting a saline groundwater end-member and from variabilities of radium isotopes in coastal aquifers (Beck et al., 2007; Garcia-Solsona et al., 2010; Liu et al., 2012). Therefore, the spatial distribution and temporal variation of radium isotopes under various influencing factors are of significance to gain insights into the reactive transport of radium isotopes in coastal aquifers and are also essential for accurately estimating SGD flux and SGD associated chemical loadings to the ocean.

The sources (+) and sinks (−) of radium isotopes in coastal groundwater include physical and geochemical processes such as advection (+/−), weathering (+), decay (−), α-recoil (+), co-precipitation (−), and adsorption (−)/desorption (+) (Porcelli, 2008; Swarzenski, 2007; Tricca et al., 2000, 2001). In the coastal groundwater mixing zone (CGMZ), fresh groundwater mixes with circulated seawater driven by tidal fluctuation and density differences forming an upper saline plume (USP) and a salt wedge (SW), respectively (Liu et al., 2016; Robinson et al., 2007). The physical and chemical processes influencing the sources and sinks of radium isotopes in the CGMZ vary greatly in both spatial and temporal aspects. For example, the land-sea hydraulic gradient oscillates with diurnal/semidiurnal tidal fluctuations, spring-neap tidal cycles, and seasonal hydrologic variation. Subsequently, the shift of land-sea hydraulic gradients alters the advection of groundwater to the sea (Heiss & Michael, 2014; Liu et al., 2016). The variation of advection definitely

influences the supply and removal of radium isotopes in groundwater and subsequently affects the spatial distribution of radium isotopes in the CGMZ.

In addition, redox conditions, salinity, and pH in the CGMZ shift with tidal fluctuation (Charette & Sholkovitz, 2006; Liu et al., 2017a). Even though variations of redox conditions, salinity, and pH would not influence the physical processes such as decay and α-recoil, solid-solution partitioning of radium isotopes is very sensitive to oscillation of redox conditions, salinity, and pH (Beck & Cochran, 2013; Gonneea et al., 2008). Radium isotopes in coastal groundwater are found to increase with salinity due to the rise of ionic strength in groundwater (Kiro et al., 2014; Swarzenski, 2007; Webster et al., 1995). In addition, through controlling cation sorption, pH affects partitioning of radium isotopes substantially. A positive correlation between pH and the radium partitioning coefficient (K_d = solid-phase Ra/liquid-phase Ra) was discovered in laboratory experiments (Beck & Cochran, 2013; Gonneea et al., 2008). Compared to salinity and pH, temperature has a minor effect on partitioning and mobility of radium isotopes in coastal groundwater because adsorption enthalpies of radium vary around zero in environments such as CGMZs (Beck & Cochran, 2013; Moore, 2010).

In addition to redox conditions, salinity, and pH, the chemical composition of groundwater also impacts the partitioning of radium isotopes in coastal groundwater. The high concentration of Ba and Fe in solution hinders the adsorption of radium isotopes due to their competitive adsorption properties as indicated by Koulouris (1996). However, competitive adsorption between Fe (or Ba) and Ra was not observed in sorption competition experiments of Beck and Cochran (2013). Their results show that the existence of Ba in solution would affect Ra partitioning. However, the change of Ra partitioning is caused by coprecipitations of Ra with Ba (mainly $BaSO_4$) instead of by competitive adsorption of Ba^{2+} and Ra^{2+}. This conclusion is supported by many other studies in the literature (Kiro et al., 2013, 2012, 2015; Paytan et al., 1996). Furthermore, the geochemical cycling of manganese and iron in the CGMZ significantly alters the solubility and amount of manganese and iron oxides in the aquifer (Roy et al., 2010, 2011), and plays an essential role in the partitioning of radium isotopes in coastal groundwater due to the strong affinity of radium isotopes to manganese and iron oxides (Charette & Sholkovitz, 2006; Gonneea et al., 2013).

Apart from physical and chemical variations in solution (groundwater), properties of substrates (sediments) are also of great importance for radium partitioning between solid and liquid phases. The surface area of sediments is one of the primary controlling factors on radium partitioning in coastal groundwater. Usually, sediments with a higher abundance of clay minerals and a smaller grain size have a larger surface area and consequently have a stronger affinity to radium isotopes (Beck & Cochran, 2013). Meanwhile, the mineralogical composition of sediments is another key influencing factor of radium partitioning in groundwater because radium isotopes have dissimilar affinities to different minerals. For example, ferrihydrite has a radium partitioning coefficient two orders of magnitude larger than goethite even though both of them are iron oxides (Beck & Cochran, 2013).

Because physical and chemical interactions between sediments and groundwater affect radium partitioning in groundwater, the activity of radium isotopes in groundwater would have implications for these interactions and could be applied to evaluate mass transfer across the sediment-water interface. Tricca et al. (2001) provided a 1-D reactive transport model to comprehensively evaluate the transport of U-series and Th-series radionuclides in an unconfined aquifer considering substantial interaction between solid and liquid phases. Through simulating radium isotopes in a vertical profile with a model combining advection (or diffusion), decay, and adsorption/desorption, Krest and Harvey (2003) calculated groundwater advection or diffusion velocities and subsequently quantified the recharge and discharge of groundwater. Similarly, through reactive transport modeling of radium isotopes in pore water beneath an estuarine lagoon, the significance of transport processes such as molecular diffusion and bioturbation that control the benthic flux were stressed by Hancock et al. (2000). Through 2-D reactive transport modeling of radium isotopes, Kiro et al. (2012) presented a spatial distribution of radium isotopes in a coastal aquifer and investigated behaviors of radium isotopes under multiple influencing factors such as salinity and groundwater velocity. Different from previous studies, Cai et al. (2012) proposed a new method to investigate the mass exchange across the sediment-water interface by evaluating the disequilibrium between ^{224}Ra and ^{228}Th on bulk sediments. This method was successfully applied to studies investigating solute transfer across the sediment-water interface and benthic chemical flux (dissolved inorganic carbon, nutrients, and mercury) in salt marshes (Shi et al., 2018) or at the bottom of estuaries such as Yangtze River Estuary (Cai et al., 2014), Pearl River Estuary (Cai et al., 2015), and Jiulong River Estuary (Hong et al., 2017).

To better understand the variation of radium isotopes in coastal groundwater systems, Michael et al. (2011) characterized spatial patterns of radium isotopes in groundwater system of Waquoit Bay. Their results clearly indicated that groundwater had distinct patterns due to different driving forces. The distinct residence time scale, aquifer heterogeneity, shift of groundwater flow path, and hydrologic variation in each groundwater pattern result in different spatial patterns of radium isotopes with very dissimilar radium activities. The large variation of radium activity in coastal groundwater patterns presents a big challenge for using radium isotopes to estimate SGD flux. Therefore, it is of great importance to study the detailed spatial distribution of radium isotopes (^{224}Ra, ^{223}Ra, and ^{228}Ra) in the CGMZ, especially different behaviors of radium isotopes in the USP and SW. Moreover, temporal variations of radium isotopes at different tidal stages may provide new insights into influences of tidal fluctuation on hydrodynamics and geochemical processes in the USP and SW. This study investigates the mechanism of how tidal fluctuation influences the spatial distribution and temporal variation of radium isotopes in both the USP and SW. Distinct behaviors of radium isotopes in the USP and SW are also investigated. To achieve this objective, groundwater samples were collected from different locations in the CGMZ at different tidal stages for laboratory analysis of radium isotopes (^{224}Ra, ^{223}Ra, and ^{228}Ra), redox conditions, carbons, nutrients, and trace metals. The findings of this study may provide better understandings of supply, removal, and reactive transport of radium isotopes and offer insights into geochemical reactions in the USP and SW.

2. Materials and Methods

2.1. Study Area and Study Site

Tolo Harbor (surface area: 52 km^2; coastline: 82 km), seated at the northeastern of New Territories, Hong Kong (Figure 1a), is an embayment with a bottle-necked configuration stretching in northeast direction (Lee et al., 2012; Liu et al., 2017a; Luo et al., 2014). The catchment of Tolo Harbor is bounded by a series of mountain blocks and has an area of 160 km^2. According to the geological map (Figure 1a), bedrock in the Tolo harbor area is mainly volcanic rocks and some Devonian-Permian sedimentary rocks at the north of Tolo Channel (Figure 1b). Six rivers (SM River, TPK River, TP River, LT River, TT Stream, and SL Stream in Figure 1b) in the catchment discharge to the harbor with a rate of $\sim$0.247 cm d^{-1} (Lee et al., 2012; Liu et al., 2018). In addition to river discharge, SGD, with a rate of 0.8–11.8 cm d^{-1} (Luo & Jiao, 2016), is another pathway by which meteorological water flows back to the sea. The annual precipitation in the study area is 2,020 mm with most rainfall occurs during May and October (Liu et al., 2017b). The semidiurnal tide in Tolo Harbor has an average tidal range of $\sim$1.06 m and the mean sea level is $\sim$1.45 mPD (meter above principal datum). The specific study site (22°28′06.91″N, 114°13′02.22″E) is located at a sandy beach of Plover Cove, Tolo Harbor (Figure 1b). The sandy beach has an extremely gentle slope (1%) and the hydraulic conductivity of surficial sediments was measured to be 4.49 m d^{-1} in situ through a falling head test (Li et al., 2010; Liu et al., 2018). The porosity was measured to be $\sim$0.3 in the laboratory following standard procedures described in Fetter (2000). Based on grain size analysis, the sediments are classified as well graded gravelly sands according to the Unified Soil Classification System (Liu et al., 2018).

2.2. Sampling Strategy

A permanent multilevel sampling system (Luo et al., 2017) was installed in the intertidal zone of a sandy aquifer at Plover Cove. The system contains 11 sampling sites (named L1–L5 and S1–S6) with 2–5 sampling tubes in each site (Figure 1c). The detailed vertical and horizontal locations of each sampling tube in the aquifer can be found elsewhere (Liu et al., 2017b). In addition, a well (D4) with an automatic monitoring transducer (Cera-Diver, Schlumberger Water Service) was installed at 120 m seaward from the mean tidal mark to record the time series of tidal level with a temporal resolution of 20 min (Figure 1c). Another well (D2) was installed near sampling site L2 to monitor groundwater level variation (Figure 1c). The field trip was conducted between 23 May and 25 May 2016 and 15 rounds of groundwater sampling were conducted every 3–4 h within two tidal cycles (48 h). The exact time of each sampling round (called SR hereafter) and the corresponding sea level are illustrated in Figure 2. The sampling time of each SR was well distributed in different tidal stages in the two tidal cycles. Tidal level was above the beach surface of L2 and L3 for SRs 06, 07, 13, and 14 while tidal level was below the beach surface of L2 and L3 during other SRs. The tidal level was below the beach surface of L1 throughout the sampling period. During each SR, nine groundwater samples with a volume of 1–1.85 L each were collected from the three sampling sites located in the transition zone (L1, L2, and L3 in Figure 1c) while one nearshore seawater (NSW) sample with a volume of 4 L was
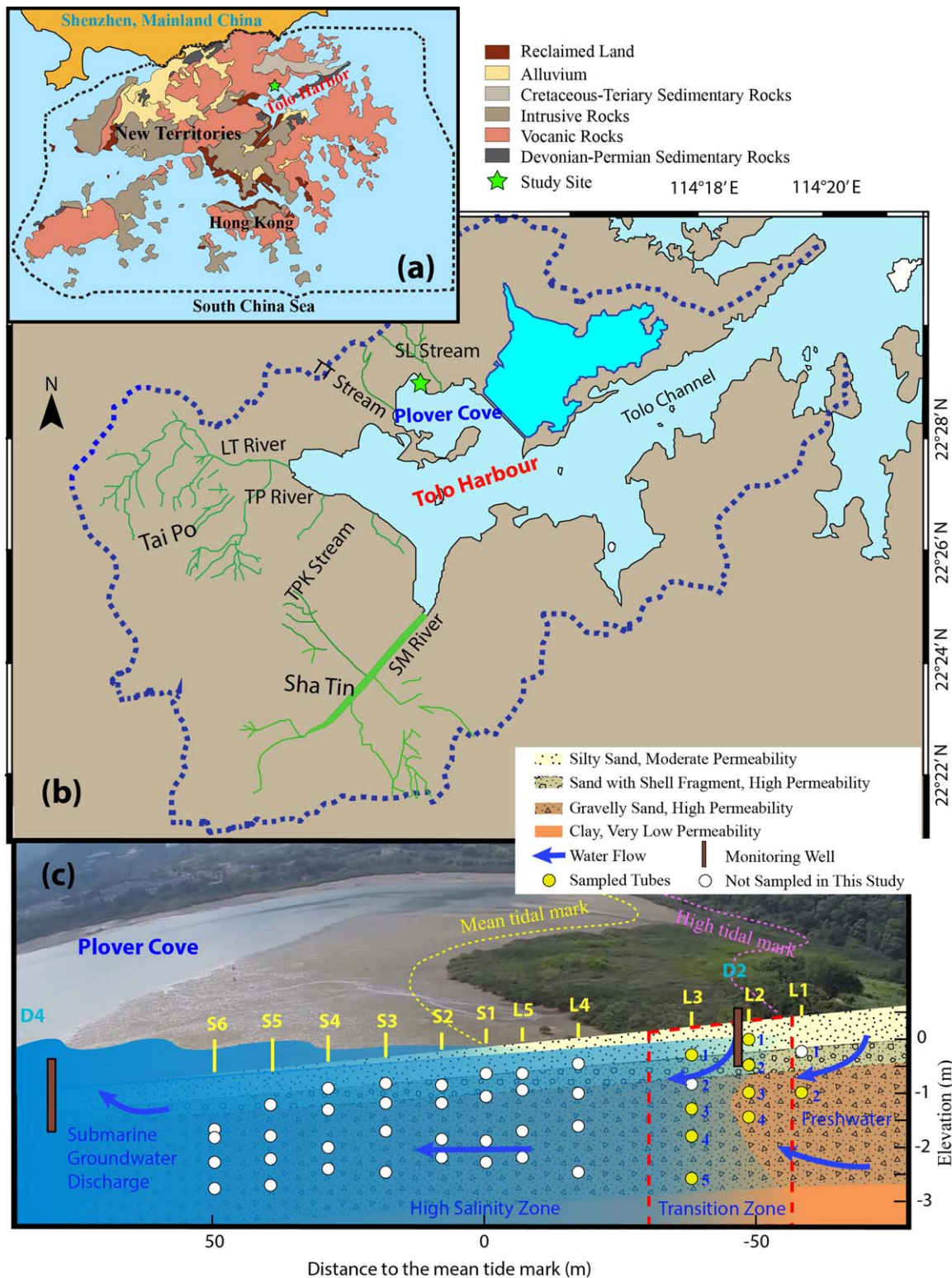
Figure 1. (a) Location of Tolo Harbor and geological map of Hong Kong, (b) the catchment and river net of Tolo Harbor, (c) the setup of sampling tubes and automatic monitoring wells in the intertidal aquifer at the study site.

collected. The groundwater and NSW samples for nutrients (50 mL) were prefiltered with a 0.45 μm syringe filter and stored in an ice box in the field and then in frozen environments (−18°C) in laboratory. HNO$_3$ was added to trace metal samples (50 mL) after the filtration to prevent precipitation and then the samples
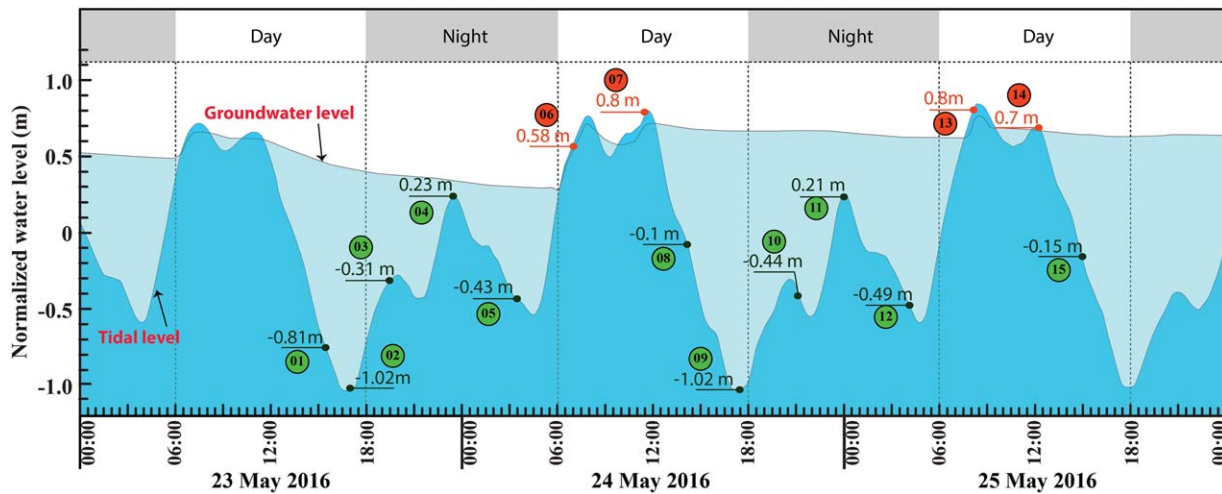
Figure 2. The tidal level (observed from D4) and groundwater level (observed from D2) variations during the sampling period and the exact time of each sampling round. The red color of sampling round number denotes that the tidal level submerges the sampling site L2 and L3 while the green color of sampling round number represents that the earth surfaces of L2 and L3 are not submerged by seawater.

were stored in refrigeration environments (4°C). In the field, samples (0.5–1.5 L) for radium isotopes (^{224}Ra, ^{223}Ra, and ^{228}Ra) were pumped first through a column filter (1 μm) to eliminate particles. Then, the filtered sample was pumped through a column loosely filled with MnO_2-coated fiber (Mn-fiber) using peristaltic pumps with a flow rate <1 L min^{-1} to extract radium isotopes by adsorption onto MnO_2 particles (Moore, 2008).

2.3. Analytical Methods

Salinity, pH, and oxidation/reduction potential (ORP) of water samples were measured in situ using a portable multiparameter meter (Hanna HI 98194, HANNA instruments) immediately after sample collection. The calibration and measurement procedures of salinity, pH, and ORP can be found in Liu et al. (2017a), and resolutions and accuracies of salinity, pH, and ORP are 0.01 and ±0.01 psu, 0.01 and ±0.02 pH, and 0.1 and ±1.0 mV, respectively. The total alkalinity was measured by a colorimetric method with a 1.6 N H_2SO_4 acid immediately after sample collection and filtration. Total alkalinity and pH were applied to the program CO2SYS (Cao et al., 2011) to calculate carbonate components such as dissolved inorganic carbon (DIC), and pCO_2. The detailed calibration and analysis procedures of nutrients (NH_4^+, NO_2^-, NO_3^-, and PO_4^{3-}) via a flow injection analyzer (FIA) were described in Liu et al. (2017c) and analytical errors are <10% for NH_4^+, <8% for NO_2^-, <3% for NO_3^-, and <5% for PO_4^{3-}. Trace metals (Fe^{2+}, Mn^{2+}, and Sr^{2+}) were analyzed by a inductively coupled plasma optical emission spectrometer (ICP-OES) with accuracies and precisions better than 4.7% and 4.8% for Fe^{2+}, 7.9% and 2.1% for Mn^{2+}, and 5% and 4.5% for Sr^{2+}, respectively. The details of calibration and measurement procedures were presented elsewhere (Liu, 2017). The prepared radium isotopes sample (Mn-fiber) was placed in a closed loop of a radium delayed coincidence counter (RaDeCC) system (Moore & Arnold, 1996) where the radon decayed from radium isotopes on the Mn-fiber was carried by helium gas to measure the activity of ^{224}Ra within 3 days after sample collection. The sample was recounted 10 and 25 days later to measure ^{223}Ra and ^{228}Th, respectively. The activity of ^{228}Th was applied to correct ^{224}Ra activity. The mechanism and standard measurement procedures of the RaDeCC system are described in Moore and Arnold (1996) and Moore (2008). About 1 year later, the long-lived radium isotope (^{228}Ra) was also measured with the RaDeCC system following the standard procedure described in Moore (2008). The uncertainties associated with the measurement of radium isotopes via the RaDeCC system were estimated according to Garcia-Solsona et al. (2008).

3. Results

3.1. Redox Conditions and Water Patterns

Four water patterns, i.e., surficial fresh groundwater (FGW), deep FGW, saline water, and NSW were identified in this study according to stable isotopic compositions (δ^2H and δ^{18}O) and salinity as described in Liu
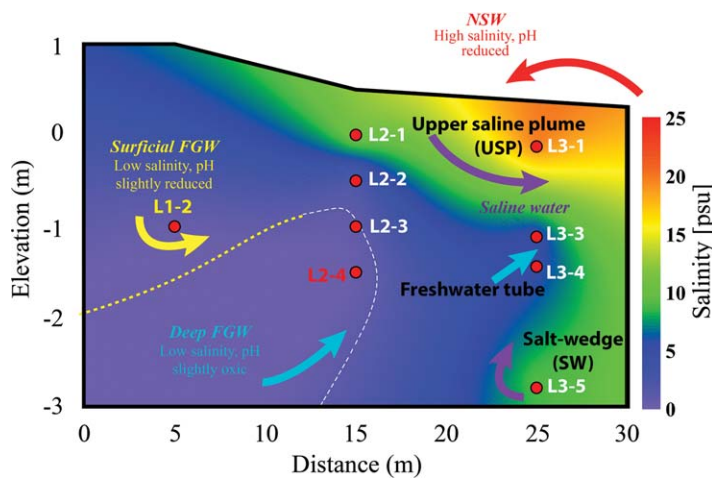
Figure 3. A sketch of water patterns in the CGMZ and general redox conditions in each water pattern. FGW is the abbreviation of fresh groundwater, NSW is the abbreviationo of nearshore seawater.

et al. (2017c) while redox conditions in these water patterns were presented and discussed in Liu et al. (2017a). As shown in Figure 3, a brief introduction to water patterns and redox conditions is given. (1) Surficial FGW (L1–2) has a low salinity (~0.2 psu) and a comparatively low pH (~6.85), and is slightly reduced with an ORP value of −30.5 mV. (2) Deep FGW (L2–4) has a higher salinity (~0.25 psu) but a lower pH (~6.38) than surficial FGW. It is worth noting that deep FGW is oxic with an ORP of 12.19 mV, which is very different from surficial FGW. (3) The NSW, with an average OPR of −55.31 mV, is more reduced than surficial FGW, but the salinity (~24.49 psu) and pH (~8.21) of which are much higher than that of surficial FGW. (4) As a mixture of aforementioned water patterns, saline water (L2-1 to L2–3, L3-1 to L3–5) has a salinity ranging from 0.83 to 19.91 psu, a pH changing from 6.32 to 6.95, and an ORP varying from −8.99 to −233.81 mV. Notably, saline water in the near-surface area (L2-1 and L3-1) is extremely reduced with very negative ORP values (−164.95 and −233.81 mV). Saline waters with comparatively high salinities at L3-1 (~19.91 psu) and L3–5 (~9.03 psu) are separated by comparatively fresh water at L3-3 and L3–4 (~6.03 and ~5.52 psu). Therefore, saline water at L2-1, L2-2, L2–3, and L3-1 is from the USP driven by tidal fluctuation whereas saline water at L3–5 is from the SW driven by density differences. This can also be supported by different stable isotopic compositions (δ^2H and δ^{18}O) of the two groups of saline waters (Liu et al., 2017c). δ^2H and δ^{18}O of groundwater from the USP (L2-1: −14.47‰ and −3.06‰) are less negative than those of groundwater from the SW (L3–5: −27.69‰ and −4.53‰) even though they have similar degrees of mixing with seawater (salinity: 10.12 versus 9.69 psu). All the aforementioned redox data can be found in the supporting information.

3.2. ^{224}Ra Dynamics

Figure 4 shows the dynamics of ^{224}Ra within two tidal cycles. Spatially, ^{224}Ra activity in both surficial (L1–2) and deep (L2–4) FGWs is low (0.86 ± 0.70 and 0.64 ± 0.32 dpm/L, respectively in Table 1) due to a large partitioning coefficient of radium isotopes in freshwater environments. With the increase of ionic strength in saline water, ^{224}Ra desorbs from the surface coating of sediments and results in a dramatic increase of ^{224}Ra activity in saline water. Consequently, ^{224}Ra activity in saline water (24.65 ± 19.79 dpm/L in Table 1) is 28–38 times of that in FGW. However, the highest ^{224}Ra activity is observed at L3–5 (65.03 ± 6.40 dpm/L) instead of L3-1 (35.31 ± 4.90 dpm/L) even though groundwater at L3-1 has the highest salinity (Table 1). This is because the rise of ^{224}Ra at L3-1 induced by desorption along with salinity increase cannot counteract the mixing loss with low ^{224}Ra seawater. Another reason is that the groundwater residence time is much longer at L3–5 (SW) than L3-1 (USP) leading to a higher ^{224}Ra activity at L3–5. In NSW, ^{224}Ra activity is 9.00 ± 4.57 dpm/L (Table 1), which is much higher than ^{224}Ra activity in FGW due to the discharge of high ^{224}Ra groundwater. Meanwhile, ^{224}Ra activity in NSW is much lower than that in saline water because of the mixing loss with offshore seawater. Temporally, owing to multiple factors influencing the enrichment and removal of ^{224}Ra in coastal groundwater, the synchronous variation of ^{224}Ra with tidal fluctuation is not obvious. However, some clues can be inferred from the temporal variation of ^{224}Ra (Figure 4). For example, ^{224}Ra activity in the near-surface area decreases drastically from SR 05 to SR 06 (from 41.67 ± 0.92 to 22.21 ± 0.62 dpm/L at L3-1 in Table 2) indicating a significant mixing loss (~36%) induced by NSW infiltration during SR 06. The decrease of ^{224}Ra activity in the near-surface area can also be observed from SR 12 to SR 13 when ^{224}Ra activity at L3-1 drops from 39.78 ± 0.87 to 37.96 ± 0.78 dpm/L while ^{224}Ra activity at L2-1 declines from 23.82 ± 0.58 to 46.46 ± 0.45 dpm/L (Table 2). Moreover, the rise of ^{224}Ra activity from SR 06 to SR 07 suggests the ingrowth of ^{224}Ra with the increase of groundwater residence time in the aquifer (Figure 4). With the drop of tidal level between SR 07 and SR 09 (0.80 to −1.02 m), the seaward flow of FGW from inland area dilutes ^{224}Ra activity in saline water in the near-surface area; during the same period the decrease of salinity, from 18.2 to 12.57 psu for L2-1 and from 21.12 to 19.98 psu for L3-1 (Liu et al., 2017a), enhances the adsorption processes of ^{224}Ra. Consequently, both processes decrease ^{224}Ra activity in saline water. For example, from SR 07 to SR 09, ^{224}Ra activity drops from 37.34 ± 0.83 to 33.63 ± 0.75 dpm/L at L3-1 and from 19.24 ± 0.53 to 17.87 ± 0.53 dpm/L at L2-1, respectively (Table 2). The aforementioned
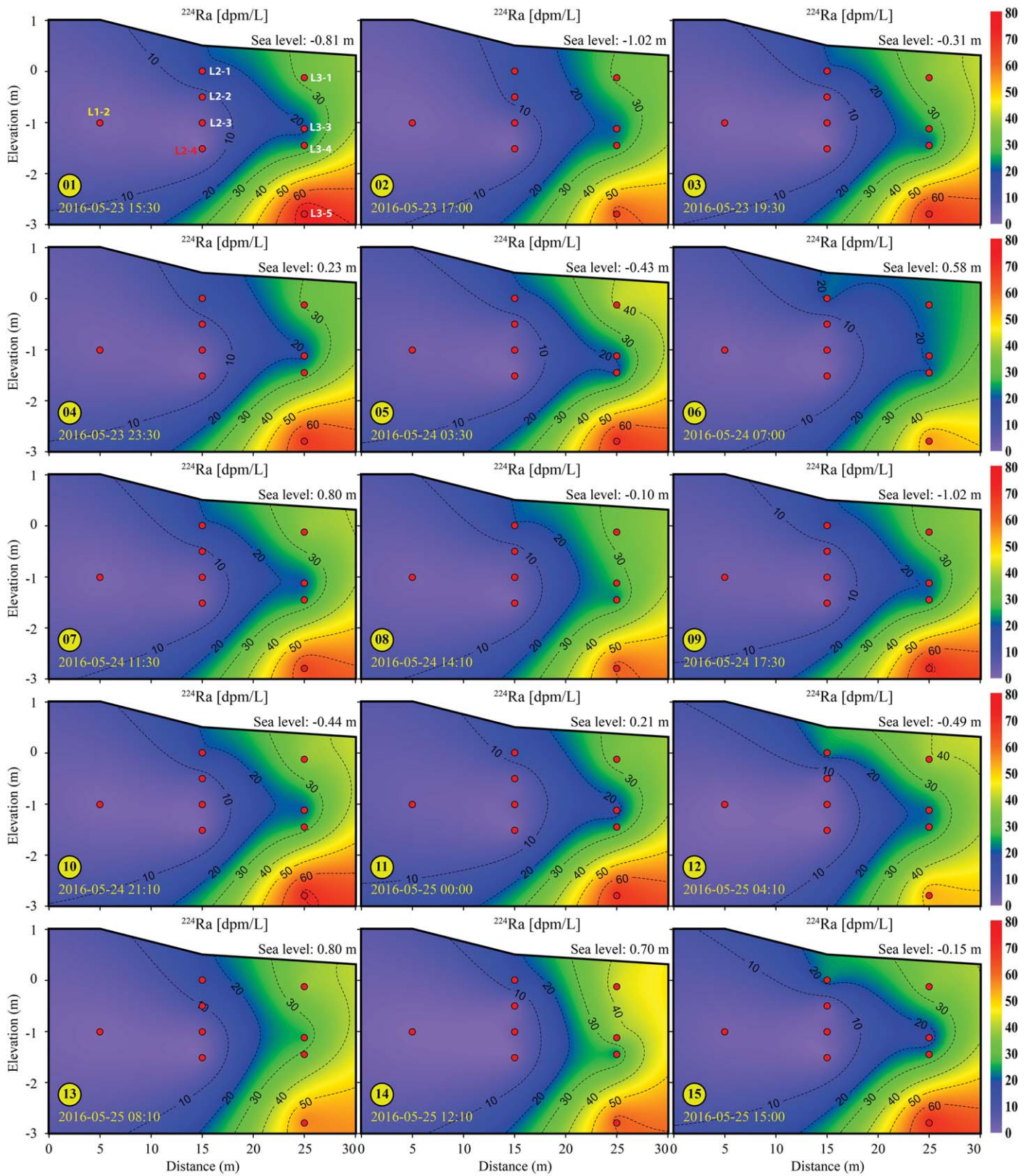
Figure 4. The spatial distribution of ^{224}Ra in groundwater of the CGMZ during different sampling rounds.

Table 1
The Average Activities and Isotopic Ratios of Radium Isotopes in Groundwater at Different Locations of the CGMZ and in Different Water Patterns During the Sampling Period

Locations and water pattern	Radium isotopes (dpm/L)						$^{224}Ra/^{228}Ra$	$^{223}Ra/^{228}Ra$
	^{224}Ra	Std[a]	^{223}Ra	Std	^{228}Ra	Std		
L1–2	0.86	0.70	0.11	0.04	0.50	0.47	1.72	0.220
L2-1	18.28	3.02	0.51	0.21	10.67	2.54	1.71	0.048
L2-2	5.78	3.00	0.13	0.07	4.03	2.77	1.43	0.032
L2–3	2.83	0.58	0.05	0.04	2.17	0.60	1.30	0.023
L2–4	0.64	0.32	0.02	0.02	0.16	0.15	4.00	0.125
L3-1	35.31	4.9	0.96	0.24	17.09	2.89	2.07	0.056
L3-3	22.32	5.14	0.43	0.37	22.37	4.35	1.00	0.019
L3–4	23.01	2.74	0.33	0.18	22.16	3.21	1.04	0.015
L3–5	65.03	6.40	0.76	0.25	69.94	6.29	0.93	0.011
Surficial FGW	0.86	0.70	0.11	0.04	0.50	0.47	1.72	0.220
Deep FGW	0.64	0.32	0.02	0.02	0.16	0.15	4.00	0.125
Saline water	24.65	19.79	0.44	0.36	24.65	19.79	1.00	0.018
NSW	9.00	4.57	0.15	0.05	4.46	2.06	2.02	0.034

[a]Standard deviation.

phenomena in the near-surface area are also observed at the second tidal cycle. The variation of ^{224}Ra in the SW (L3–5) is contrast with that in the near-surface area because of a lag of hydrodynamics in response to the shift of tidal level. In general, high ^{224}Ra activity at L3–5 is usually observed during low tidal levels that follow the highest tidal levels, such as during SRs 01, 02, and 09 when the tidal levels were -0.81, -1.02, and -1.02 m, respectively (Figure 4). The corresponding ^{224}Ra activities at L3–5 were 74.94 ± 2.43, 69.47 ± 2.15, and 70.68 ± 1.59 dpm/L, respectively (Table 2), which are much higher than the average ^{224}Ra activity at L3–5 during the sampling period (65.03 dpm/L in Table 1).

3.3. ^{223}Ra Dynamics

The spatial distribution of ^{223}Ra (Figure 5) is similar to that of ^{224}Ra in the CGMZ (Figure 4). Four aspects of the distribution are notable. (1) Due to the adsorption to sediment surface coatings, ^{223}Ra activity in both surficial (0.11 ± 0.04 dpm/L) and deep (0.02 ± 0.02 dpm/L) FGWs is very low (Table 1). (2) ^{223}Ra activity in saline water increases with salinity. For example, while salinity rises from 0.83 psu at L2–3 to 13.29 psu at L2-1 (Liu et al., 2017a), ^{223}Ra activity climbs from 0.05 ± 0.04 to 0.66 ± 0.33 dpm/L accordingly (Table 1). (3) ^{223}Ra activity in the near-surface area is diluted due to NSW infiltration with low ^{223}Ra activity at high tide such as during SR 06 and SR 13 (Figure 5). For example, ^{223}Ra activity at L3-1 drops from 0.92 ± 0.03 dpm/L during SR 05 to 0.80 ± 0.02 dpm/L during SR 06 while ^{223}Ra activity at L2-1 declines from 0.85 ± 0.03 to 0.24 ± 0.01 dpm/L during the same period (Table 2). (4) Owing to the decay of mother nuclide (^{227}Th, $t_{1/2} = 18.7$ days), ^{223}Ra activity recovers several hours after the mixing loss induced by NSW infiltration (Figure 5). For instance, ^{223}Ra activity at L2-1 rises from 0.24 ± 0.01 dpm/L during SR 06 to 0.61 ± 0.03 dpm/L during SR 07 while it climbs from 0.18 ± 0.01 dpm/L for SR 13 to 0.55 ± 0.02 dpm/L for SR 14 (Table 2).

It is worth noting that there are some dissimilarities in spatial distributions of ^{223}Ra and ^{224}Ra due to their differences in relative ingrowth rates (defined as the ratio between net production rates and equilibrium activity) in the aquifer. First, average activity of ^{223}Ra is higher at L3-1 than at L3–5 (0.96 ± 0.24 versus 0.76 ± 0.25 dpm/L in Table 1). Meanwhile during the majority of SRs (e.g., SRs 01, 02, 04, 05, 07, 08, 09, 10, 11, 12, and 14), ^{223}Ra is higher at L3-1 than L3–5 (Figure 5). The major reason for this unique distribution of ^{223}Ra at L3-1 and L3–5 is that the ingrowth rate of ^{223}Ra is large enough to support ^{223}Ra to reach secular equilibrium in a short time owing to the short half-life of ^{227}Th. Therefore, the total exchangeable ^{223}Ra (both dissolved and adsorbed phases) is very high for both L3-1 and L3–5. Since salinity is much higher at L3-1 than at L3–5 (19.91 versus 9.03 psu) the ^{223}Ra partitioning coefficient would be smaller at L3-1 than at L3–5. Consequently, more ^{223}Ra exits in dissolved phase at L3-1 than at L3–5, even though groundwater at L3-1 suffers from a mixing loss and has a shorter residence time than that at L3–5. If groundwater salinity in the near-surface area is comparable to that at L3–5, it would be expected that the activity of ^{223}Ra would be lower in the near-surface area than at L3–5 due to the mixing loss and shorter residence time at the former

Table 2
The Activities of Radium Isotopes of NSW and Groundwater During Different Sampling Rounds

| No.	Ra (dpm/L)	L1-2	L2-1	L2-2	L2-3	L2-4	L3-1	L3-3	L3-4	L3-5	NSW
SR 01	^{224}Ra	0.60 ± 0.02	18.88 ± 0.49	6.47 ± 0.20	2.60 ± 0.17	0.25 ± 0.03	32.89 ± 0.78	19.01 ± 0.48	22.78 ± 0.52	74.94 ± 2.43	11.01 ± 0.31
	^{223}Ra	0.07 ± 0.00	0.57 ± 0.03	0.18 ± 0.01	0.01 ± 0.00	0.03 ± 0.00	0.83 ± 0.02	0.38 ± 0.02	0.49 ± 0.02	0.61 ± 0.03	0.11 ± 0.01
	^{228}Ra	0.65 ± 0.04	11.86 ± 0.36	5.29 ± 0.13	2.77 ± 0.18	0.08 ± 0.01	20.88 ± 0.56	20.00 ± 0.56	22.51 ± 0.65	69.47 ± 2.15	5.19 ± 0.25
SR 02	^{224}Ra	0.31 ± 0.05	13.20 ± 0.33	12.84 ± 0.82	3.97 ± 0.08	0.64 ± 0.08	31.59 ± 0.72	21.05 ± 0.70	23.49 ± 0.62	61.65 ± 1.84	6.84 ± 0.17
	^{223}Ra	0.08 ± 0.01	0.47 ± 0.03	0.12 ± 0.01	0.03 ± 0.00	0.02 ± 0.00	0.98 ± 0.02	0.09 ± 0.01	0.40 ± 0.02	0.43 ± 0.03	0.15 ± 0.01
	^{228}Ra	0.13 ± 0.01	9.64 ± 0.29	8.01 ± 0.30	2.52 ± 0.16	0.07 ± 0.01	16.08 ± 0.43	16.86 ± 0.47	19.67 ± 0.57	64.79 ± 2.01	3.93 ± 0.19
SR 03	^{224}Ra	0.33 ± 0.05	19.22 ± 0.44	4.25 ± 0.25	2.26 ± 0.07	0.34 ± 0.02	37.03 ± 1.09	26.20 ± 0.83	20.52 ± 0.52	69.26 ± 1.46	8.22 ± 0.22
	^{223}Ra	0.12 ± 0.01	0.55 ± 0.02	0.15 ± 0.01	0.01 ± 0.00	0.03 ± 0.00	0.49 ± 0.02	0.20 ± 0.01	0.32 ± 0.01	0.69 ± 0.02	0.11 ± 0.00
	^{228}Ra	0.05 ± 0.00	11.48 ± 0.34	1.79 ± 0.07	2.31 ± 0.15	0.05 ± 0.00	12.19 ± 0.33	23.89 ± 0.67	21.62 ± 0.63	55.90 ± 1.73	8.76 ± 0.43
SR 04	^{224}Ra	1.22 ± 0.04	14.29 ± 0.35	7.71 ± 0.35	2.72 ± 0.07	0.85 ± 0.09	31.24 ± 0.83	18.76 ± 0.48	25.40 ± 0.54	68.11 ± 1.81	7.07 ± 0.20
	^{223}Ra	0.11 ± 0.00	0.42 ± 0.02	0.13 ± 0.00	0.05 ± 0.00	0.01 ± 0.00	0.85 ± 0.02	0.29 ± 0.01	0.26 ± 0.01	0.65 ± 0.03	0.10 ± 0.00
	^{228}Ra	0.68 ± 0.04	7.85 ± 0.24	2.54 ± 0.09	2.15 ± 0.14	0.59 ± 0.04	16.81 ± 0.45	19.68 ± 0.55	23.74 ± 0.69	80.66 ± 2.50	3.57 ± 0.17
SR 05	^{224}Ra	1.76 ± 0.09	17.95 ± 0.39	4.91 ± 0.14	2.84 ± 0.07	0.38 ± 0.06	41.67 ± 0.92	21.15 ± 0.58	18.42 ± 0.52	68.84 ± 1.43	10.85 ± 0.27
	^{223}Ra	0.18 ± 0.01	0.85 ± 0.03	0.12 ± 0.01	0.10 ± 0.00	0.00 ± 0.00	0.92 ± 0.03	0.43 ± 0.02	0.14 ± 0.01	0.36 ± 0.02	0.20 ± 0.01
	^{228}Ra	0.69 ± 0.05	8.49 ± 0.25	2.63 ± 0.10	2.52 ± 0.16	0.07 ± 0.01	19.68 ± 0.53	24.76 ± 0.69	17.40 ± 0.50	64.22 ± 1.99	4.99 ± 0.24
SR 06	^{224}Ra	0.89 ± 0.07	21.35 ± 0.50	3.94 ± 0.12	2.36 ± 0.13	0.51 ± 0.10	22.21 ± 0.62	21.38 ± 0.65	19.51 ± 0.69	54.04 ± 1.46	7.24 ± 0.19
	^{223}Ra	0.10 ± 0.00	0.24 ± 0.01	0.10 ± 0.01	0.00 ± 0.00	0.02 ± 0.00	0.80 ± 0.02	0.60 ± 0.02	0.24 ± 0.02	0.90 ± 0.04	0.19 ± 0.01
	^{228}Ra	0.31 ± 0.02	9.55 ± 0.29	3.28 ± 0.12	2.03 ± 0.13	0.11 ± 0.01	12.40 ± 0.33	23.56 ± 0.66	21.49 ± 0.62	75.92 ± 2.35	2.11 ± 0.10
SR 07	^{224}Ra	0.38 ± 0.05	19.24 ± 0.53	8.55 ± 0.40	3.62 ± 0.11	1.65 ± 0.08	37.34 ± 0.83	20.01 ± 0.63	23.25 ± 0.64	65.45 ± 1.99	1.70 ± 0.06
	^{223}Ra	0.04 ± 0.00	0.61 ± 0.03	0.25 ± 0.01	0.07 ± 0.00	0.06 ± 0.00	0.83 ± 0.02	0.08 ± 0.01	0.46 ± 0.02	0.71 ± 0.03	0.06 ± 0.00
	^{228}Ra	0.09 ± 0.01	7.74 ± 0.23	6.01 ± 0.55	3.34 ± 0.22	0.15 ± 0.01	14.78 ± 0.40	20.85 ± 0.58	27.92 ± 0.81	68.99 ± 2.14	1.20 ± 0.06
SR 08	^{224}Ra	1.15 ± 0.03	19.71 ± 0.53	6.42 ± 0.25	3.66 ± 0.10	0.70 ± 0.03	32.85 ± 1.04	27.33 ± 0.58	22.98 ± 0.63	61.37 ± 1.92	6.07 ± 0.15
	^{223}Ra	0.09 ± 0.00	0.49 ± 0.02	0.11 ± 0.01	0.10 ± 0.00	0.01 ± 0.00	0.91 ± 0.02	0.49 ± 0.03	0.24 ± 0.01	0.74 ± 0.02	0.17 ± 0.01
	^{228}Ra	0.28 ± 0.02	14.48 ± 0.43	4.85 ± 0.18	1.61 ± 0.10	0.06 ± 0.00	19.01 ± 0.51	21.78 ± 0.61	21.74 ± 0.63	65.56 ± 2.03	3.11 ± 0.15
SR 09	^{224}Ra	1.71 ± 0.08	17.87 ± 0.53	5.67 ± 0.16	3.36 ± 0.08	0.84 ± 0.06	33.63 ± 0.75	20.79 ± 0.53	21.53 ± 0.61	70.68 ± 1.59	21.04 ± 0.54
	^{223}Ra	0.16 ± 0.01	0.15 ± 0.01	0.10 ± 0.01	0.13 ± 0.01	0.03 ± 0.00	1.57 ± 0.03	0.89 ± 0.04	0.18 ± 0.01	1.09 ± 0.03	0.18 ± 0.01
	^{228}Ra	1.27 ± 0.08	11.75 ± 0.35	2.81 ± 0.10	3.12 ± 0.20	0.45 ± 0.03	15.51 ± 0.42	20.60 ± 0.58	21.01 ± 0.61	72.38 ± 2.24	6.34 ± 0.31
SR 10	^{224}Ra	0.36 ± 0.03	19.10 ± 0.44	6.35 ± 0.17	2.37 ± 0.09	0.77 ± 0.05	38.06 ± 0.87	20.25 ± 0.59	25.68 ± 0.66	71.07 ± 1.65	8.57 ± 0.25
	^{223}Ra	0.12 ± 0.00	0.52 ± 0.04	0.18 ± 0.01	0.07 ± 0.00	0.04 ± 0.00	1.27 ± 0.02	0.32 ± 0.02	0.13 ± 0.01	0.61 ± 0.03	0.11 ± 0.01
	^{228}Ra	0.29 ± 0.02	8.47 ± 0.25	5.46 ± 0.20	2.06 ± 0.13	0.05 ± 0.00	17.08 ± 0.46	17.13 ± 0.48	23.24 ± 0.67	67.94 ± 2.11	3.35 ± 0.16
SR 11	^{224}Ra	2.52 ± 0.06	14.06 ± 0.37	3.36 ± 0.12	3.16 ± 0.08	0.58 ± 0.04	34.40 ± 0.88	17.34 ± 0.48	23.22 ± 0.65	69.08 ± 1.63	7.15 ± 0.17
	^{223}Ra	0.05 ± 0.00	0.92 ± 0.03	0.07 ± 0.00	0.03 ± 0.00	0.02 ± 0.00	1.02 ± 0.03	0.41 ± 0.02	0.21 ± 0.01	0.99 ± 0.03	0.12 ± 0.01
	^{228}Ra	1.46 ± 0.10	8.16 ± 0.24	4.45 ± 0.16	1.46 ± 0.09	0.11 ± 0.01	15.58 ± 0.42	26.06 ± 0.73	16.88 ± 0.49	70.98 ± 2.20	2.56 ± 0.13
SR 12	^{224}Ra	0.12 ± 0.04	23.82 ± 0.58	2.49 ± 0.10	1.93 ± 0.07	0.51 ± 0.03	39.78 ± 0.87	21.48 ± 0.65	22.23 ± 0.61	52.79 ± 1.35	12.91 ± 0.31
	^{223}Ra	0.16 ± 0.01	0.56 ± 0.02	0.04 ± 0.00	0.02 ± 0.00	0.03 ± 0.00	1.10 ± 0.03	0.47 ± 0.02	0.53 ± 0.02	0.90 ± 0.05	0.24 ± 0.01
	^{228}Ra	0.01 ± 0.00	15.28 ± 0.46	1.85 ± 0.07	2.19 ± 0.14	0.26 ± 0.02	15.58 ± 0.42	22.31 ± 0.62	23.40 ± 0.68	65.31 ± 2.02	6.71 ± 0.33
SR 13	^{224}Ra	0.30 ± 0.02	16.46 ± 0.45	10.08 ± 0.27	2.56 ± 0.05	0.63 ± 0.02	37.96 ± 0.78	25.51 ± 0.69	30.57 ± 0.76	57.15 ± 1.46	4.78 ± 0.12
	^{223}Ra	0.12 ± 0.00	0.18 ± 0.01	0.28 ± 0.01	0.06 ± 0.00	0.02 ± 0.00	0.85 ± 0.03	0.68 ± 0.02	0.35 ± 0.02	1.07 ± 0.03	0.12 ± 0.00
	^{228}Ra	0.20 ± 0.01	9.07 ± 0.27	11.48 ± 0.42	1.25 ± 0.08	0.07 ± 0.01	22.50 ± 0.61	26.99 ± 0.76	29.48 ± 0.85	71.38 ± 2.21	3.03 ± 0.15
SR 14	^{224}Ra	15.95 ± 0.42	1.59 ± 0.04	2.74 ± 0.07	0.53 ± 0.02	43.08 ± 0.88	38.04 ± 0.98	22.89 ± 0.69	61.50 ± 1.60	6.09 ± 0.13	15.95 ± 0.42
	^{223}Ra	0.08 ± 0.00	0.55 ± 0.02	0.04 ± 0.00	0.01 ± 0.00	0.00 ± 0.00	0.84 ± 0.03	0.29 ± 0.02	0.09 ± 0.01	1.24 ± 0.03	0.14 ± 0.01
	^{228}Ra	0.13 ± 0.01	11.02 ± 0.33	0.82 ± 0.03	1.43 ± 0.09	0.19 ± 0.01	17.75 ± 0.48	34.02 ± 0.95	21.96 ± 0.64	75.71 ± 2.35	4.46 ± 0.22
SR 15	^{224}Ra	1.29 ± 0.04	23.07 ± 0.59	2.09 ± 0.04	2.28 ± 0.06	0.36 ± 0.05	35.92 ± 0.86	16.56 ± 0.45	22.68 ± 0.61	69.50 ± 1.83	15.50 ± 0.44
	^{223}Ra	0.14 ± 0.01	0.60 ± 0.03	0.03 ± 0.00	0.01 ± 0.00	0.00 ± 0.00	1.09 ± 0.02	0.04 ± 0.01	0.34 ± 0.02	0.45 ± 0.02	0.22 ± 0.01
	^{228}Ra	1.27 ± 0.08	15.17 ± 0.45	0.86 ± 0.03	1.72 ± 0.11	0.08 ± 0.01	20.48 ± 0.55	17.10 ± 0.48	20.36 ± 0.59	79.86 ± 2.48	7.56 ± 0.37
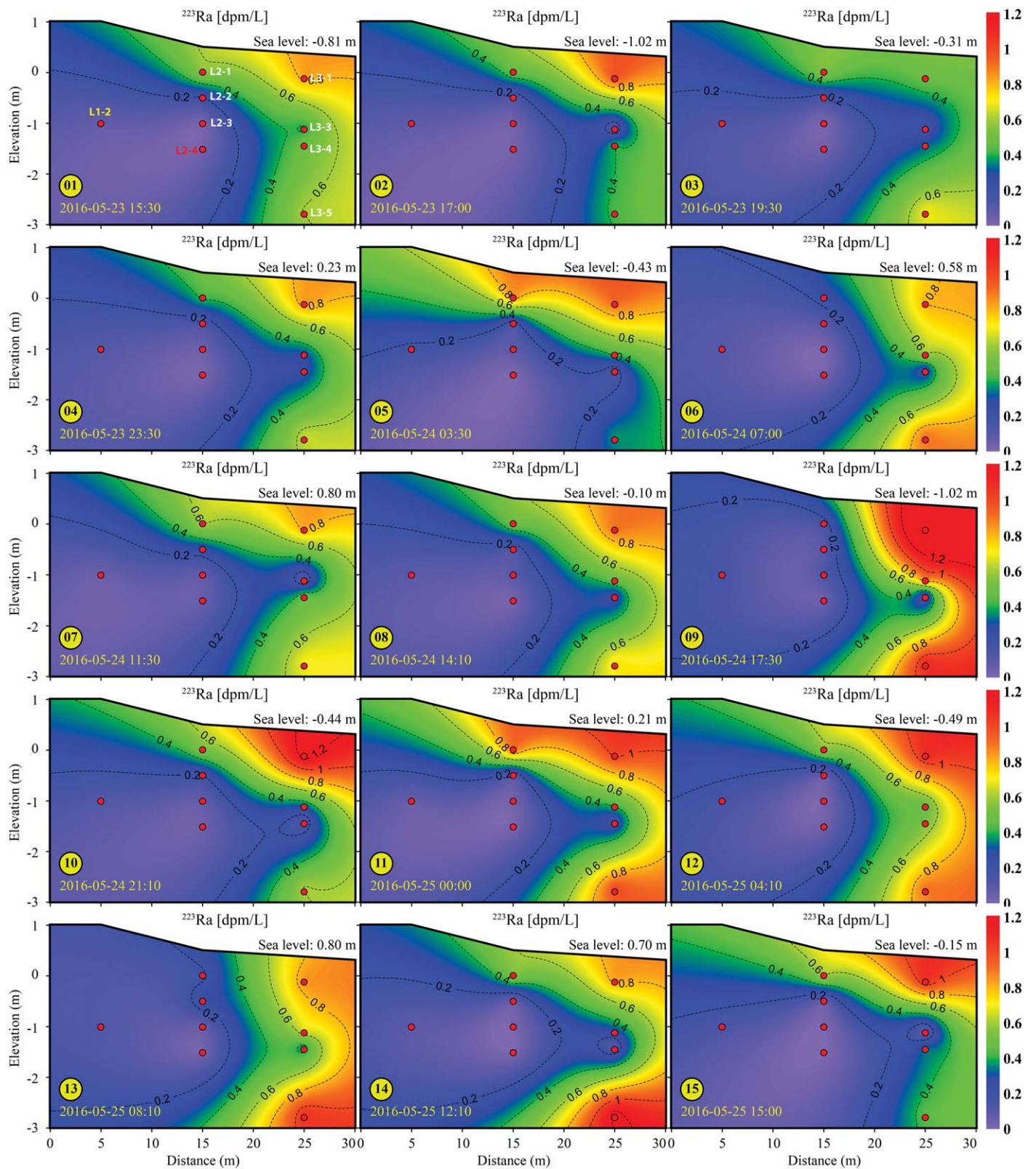
Figure 5. The spatial distribution of ^{223}Ra in groundwater of the CGMZ during different sampling rounds.

location. This can be demonstrated by the fact that [223]Ra activity is lower at L2-1 than at L3–5 (0.51 ± 0.21 versus 0.76 ± 0.25 dpm/L in Table 1), even though groundwater salinities at the two locations are similar (~10 versus ~9 psu) (Liu et al., 2017a).

3.4. [228]Ra Dynamics

In one respect, [228]Ra and [224]Ra, have very similar chemical properties because both of them belong to the same decay chain; however, they behave differently during transport in an aquifer due to their dissimilarities in production rates and half-lives. Therefore, the spatial distributions and temporal variations of [228]Ra (Figure 6) and [224]Ra (Figure 4) have similarities and differences at the same time. Specifically, similar to [224]Ra, [228]Ra in both surficial and deep FGWs (0.50 ± 0.047 and 0.16 ± 0.15 dpm/L) is very low due to a strong adsorption to sediments in freshwater environments. Another similarity is that the highest activities of both [224]Ra (65.03 ± 6.40 dpm/L) and [228]Ra (69.94 ± 6.29 dpm/L) are observed at L3–5 (Figures 4 and 6) where groundwater is not affected by mixing loss and groundwater residence time is long. Moreover, at high tide, due to the infiltration of low [228]Ra seawater, [228]Ra activity in the near-surface area suffers significantly from mixing loss (from SR 05 to SR 06 in Figure 6). Subsequently, with the rise of groundwater residence time, [228]Ra activity in this zone recovers noticeably (from SR 06 to SR 08 in Figure 6) due to the supply induced by the decay of [232]Th in the aquifer, which is similar to the dynamics of [224]Ra. One thing that should be noted is that the time needed for recovery of [228]Ra is longer due to its smaller relative ingrowth rate in the aquifer compared to [224]Ra. Similar to [224]Ra, [228]Ra activity increases with salinity due to desorption processes in saline water. For example, [228]Ra climbs from 2.17 ± 0.60 dpm/L at L2–3 to 10.67 ± 2.54 dpm/L at L2-1 while salinity rises from 0.83 to 13.29 psu accordingly (Liu et al., 2017a). However, very different spatial distributions of [228]Ra and [224]Ra are observed in the near-surface area, especially at L3-1. Specifically, groundwater at L3-1 has a higher salinity but a lower [228]Ra activity (19.91 psu and 17.09 ± 2.89 dpm/L) compared to deeper locations such as L3-3 (6.03 psu and 22.37 ± 4.35 dpm/L) and L3–4 (5.52 psu and 23.01 ± 2.74 dpm/L) where desorption of [228]Ra is not as significant as at L3-1 (Table 1). This is because the mixing loss in the near-surface area (L3-1) is more significant and the residence time in the near-surface area (L3-1) is much shorter than in deeper locations. Under such circumstances, the total exchangeable [228]Ra is low in the near-surface area due to the low relative ingrowth rate induced by the long half-life of [232]Th ($t_{1/2}$ = 14.1 Gyr).

3.5. Radium Isotopic Ratios

The isotopic ratios between short-lived ([224]Ra and [223]Ra) and long-lived ([228]Ra) radium isotopes are illustrated in Table 1. In this study, the [224]Ra/[228]Ra ratio ranges from 0.93 to 4.0 while the [223]Ra/[228]Ra ratio varies from 0.011 to 0.220. Generally, FGW has comparatively large [224]Ra/[228]Ra and [223]Ra/[228]Ra ratios. These ratios are much smaller at L3–5 than at other locations. This is because groundwater at L3–5 has the longest residence time and all radium isotopes ([224]Ra, [223]Ra, [228]Ra) reach secular equilibrium whereas at other locations even if [224]Ra and [223]Ra reach secular equilibrium, [228]Ra is far from secular equilibrium. Therefore, the lowest [224]Ra/[228]Ra and [223]Ra/[228]Ra ratios are observed at L3–5. In addition, [224]Ra/[228]Ra and [223]Ra/[228]Ra ratios at L3-3 (1.00 and 0.019) and L3–4 (1.04 and 0.015) are very close to those at L3–5 (0.93 and 0.011) because saline water from the three locations are in the transition zone of the SW. Figure 7 clearly presents linear relationships of [223]Ra versus [224]R, and [228]Ra versus [224]Ra in the USP and SW transition zones. The slope of the linear fit of [223]Ra versus [224]Ra is much larger in the USP than SW transition zones (Figure 7a). The dissimilarities in slopes of the fitted lines represent the differences in average [223]Ra/[224]Ra ratios in the USP and SW transition zones, which are caused by different residence times of groundwater in the two zones. Specifically, when seawater enters the aquifer, the activities of both [223]Ra and [224]Ra will increase and result in a comparatively stable [223]Ra/[224]Ra ratio until [223]Ra reaches secular equilibrium. From that time on, the [223]Ra activity will be stable, however, the ingrowth of [224]Ra continues and leads to a decline of the [223]Ra/[224]Ra ratio until [224]Ra reaches secular equilibrium. After that, [223]Ra/[224]Ra ratio will be a constant value which is much lower than that before both [223]Ra and [224]Ra reach secular equilibrium. [223]Ra/[224]Ra ratio in the USP is higher than the equilibrium [223]Ra/[224]Ra ratio in locations such as L3–5. The aforementioned interpretations are also applicable to explain the dissimilar slopes of fitted lines for [228]Ra versus [224]Ra in the USP and SW transition zones (Figure 7b).
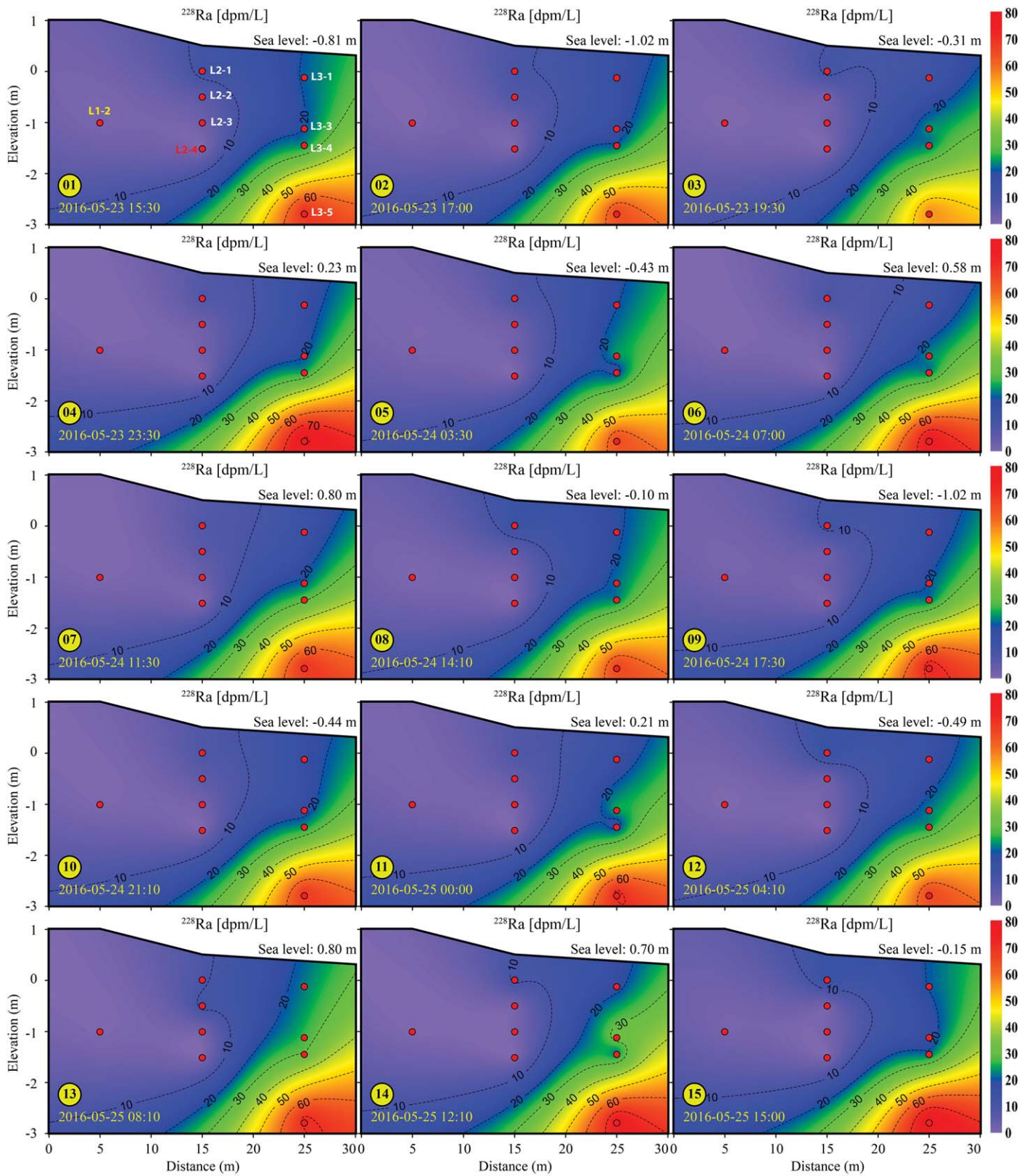
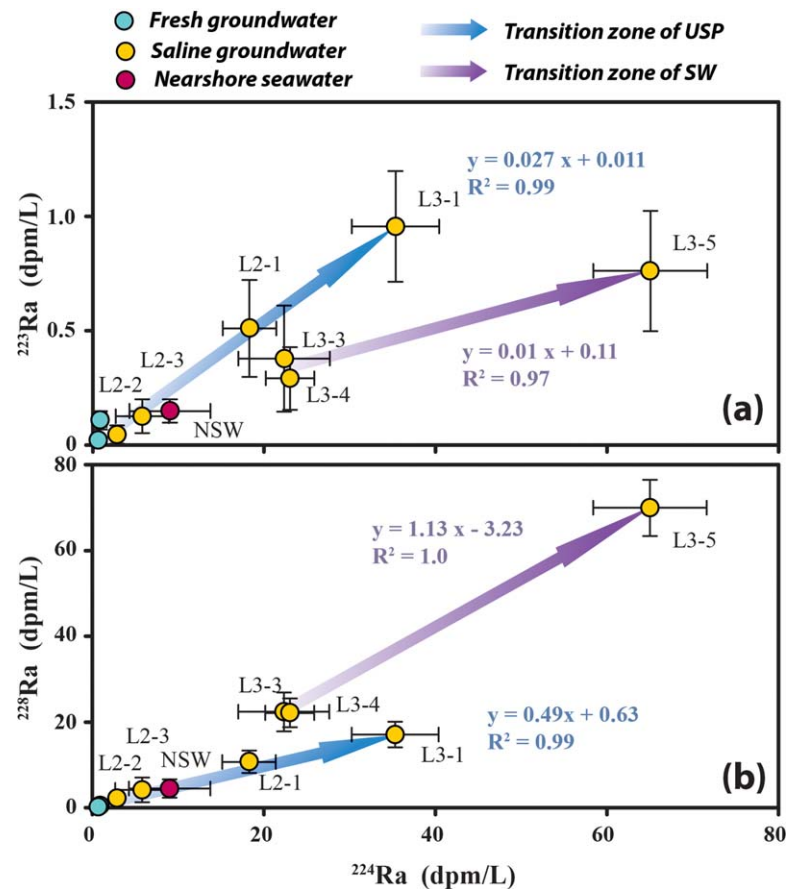**Figure 6.** The spatial distribution of ^{228}Ra in groundwater of the CGMZ during different sampling rounds.

Figure 7. The relationships of raidium isotopes. (a) ^{223}Ra versus ^{224}Ra and (b) ^{228}Ra versus ^{224}Ra.

4. Discussions

4.1. Using Radium Dynamics to Trace Hydrodynamics in the USP and SW

Figures 8 and 9 show the time series of tidal level, salinity, and radium isotopes of groundwater in the USP (L2-1) and SW (L3–5), respectively. Clearly, the effects of tidal fluctuation on salinity and dynamics of radium isotopes differ between the USP and SW due to their different depths and flow paths. Salinity and hydraulic head usually react more quickly in the USP than in the SW. For example, salinity at L2-1 (Figure 8b) lags only slightly (~0 h) behind tidal fluctuation (Figure 8a) due to the shallow depth of L2-1 and very little time for seawater to infiltrate to L2-1, whereas salinity at L3–5 (Figure 9b) lags ~12 h behind tidal fluctuation (Figure 9a) due to its long flow path and deep location. The observations in this study are consistent with previous numerical simulations and field observations (Levanon et al., 2016, 2017; Liu et al., 2016). As for the variations of radium isotopes at L2-1 (Figures 8c–8e), they show consistent trends with tidal fluctuation and salinity variation except during the high tide when radium isotopes in the near-surface area suffer from mixing loss induced by the infiltration of low radium seawater. Obviously, the time series of radium isotopes in the SW (L3–5) (Figures 9c–9e) lags behind the variation of radium isotopes in the USP (L2-1) (Figures 8c–8e), which have similar reasons for the lag of salinity in the SW (L3–5) compared to the USP (L2-1) (Figures 8b and 9b). In addition, radium isotopes in the SW (L3–5) do not show a decrease during high tide. This is because the saline water at L3–5 is upwelling circulated seawater driven by density differences (SW), and the circulated seawater has a very long residence time in the aquifer, such that radium isotopes reach secular equilibrium before seawater reaches L3–5. As for the time series of salinity (Figure 10b) and radium isotopes (Figures 10c, 10d, and 10e) in NSW, all of them show a reverse trend with tidal fluctuation (Figure 10a) because the outflow of submarine groundwater with comparatively low salinity and high activity of radium isotopes at low tide drops salinity but raises the activity of radium isotopes in the NSW and, inversely, the mixing loss by open seawater with high salinity and low activity of radium isotopes at high
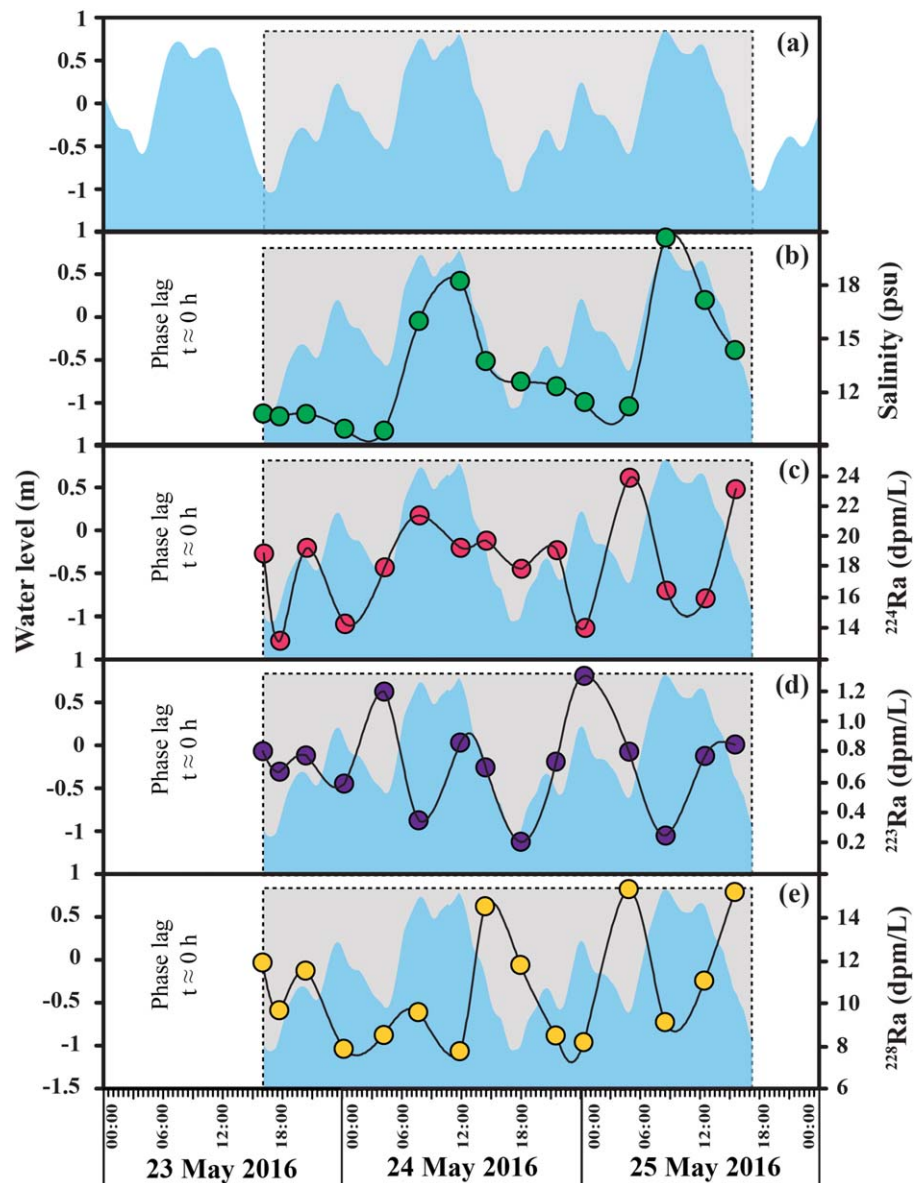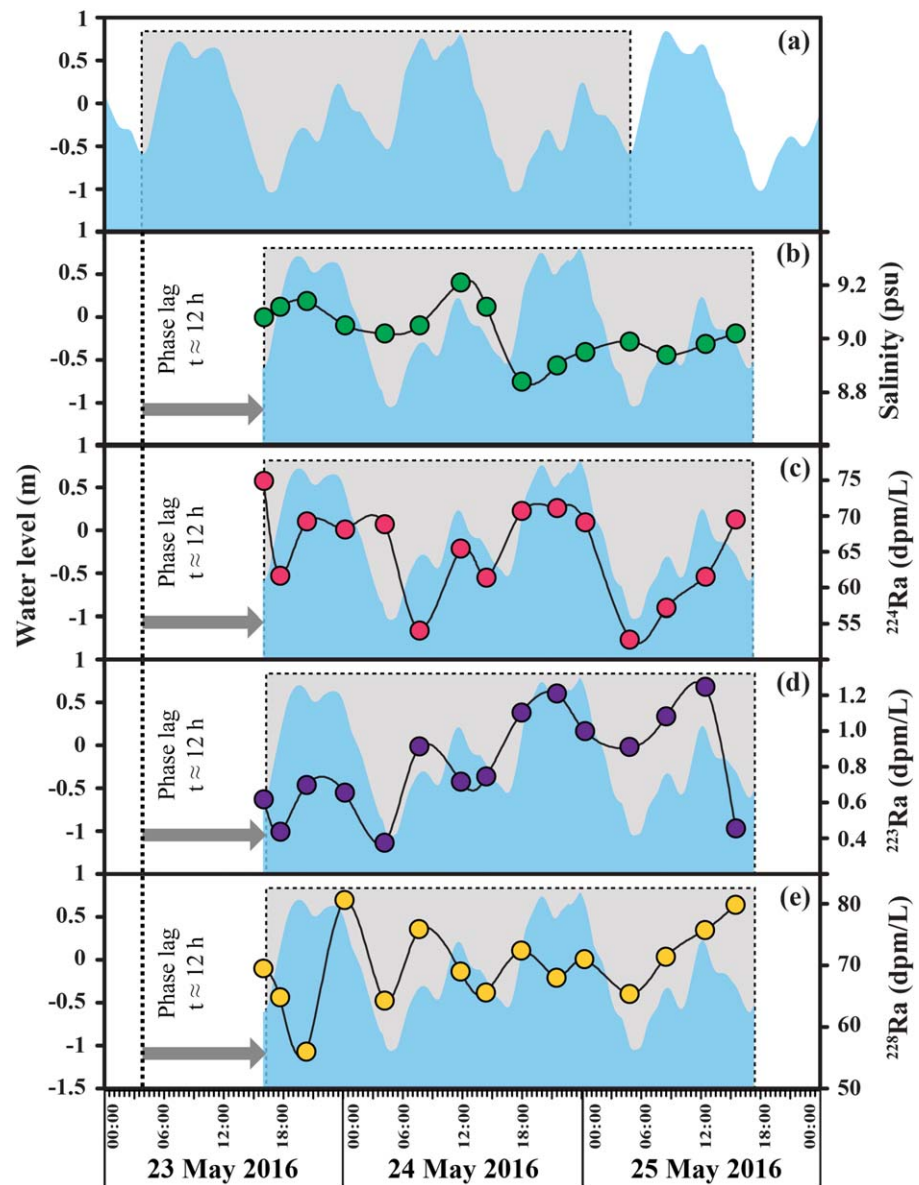
Figure 8. The variations of (a) tidal level, (b) salinity, (c) ^{224}Ra, (d) ^{223}Ra, and (e) ^{228}Ra at L2-1.

tide increases salinity but decreases the activity of radium isotopes in the NSW. The findings of this study are consistent with the observations in the German Wadden Sea (Moore et al., 2011).

4.2. Using Radium Isotopes to Trace Redox Conditions in the USP and SW

The relationship between redox indicators and ^{224}Ra shown in Figure 11 clearly suggests that the effect of redox condition on ^{224}Ra in the USP is different from that in the SW. According to Figure 11a, ^{224}Ra in both USP and SW transition zones rises with salinity due to desorption processes induced by increased ionic strength of groundwater (Kiro et al., 2014; Swarzenski, 2007; Webster et al., 1995). However, the rate of increase (slope of the fitted line in Figure 11a) is much lower in the USP than the SW. This is because the total exchangeable ^{224}Ra is lower in the USP than in the SW due to tidal flushing of the near-surface area of the USP. Therefore, even if the ^{224}Ra partitioning coefficient is the same in both the USP and the SW, the dissolved ^{224}Ra would be lower in the USP than in the SW, which results in the aforementioned lower rate of increase of ^{224}Ra in the USP. In this study, ^{224}Ra is observed to increase with pH (Figure 11b), even though the increase of pH has negative influences on the partitioning of ^{224}Ra as indicated by Beck and Cochran

Figure 9. The variations of (a) tidal level, (b) salinity, (c) ^{224}Ra, (d) ^{223}Ra, and (e) ^{228}Ra at L3–5.

(2013) and Gonneea et al. (2008). The increase of pH in this study is caused by mixing with seawater. At the same time, salinity increases, which subsequently increases the desorption of ^{224}Ra. Therefore, the negative influence on ^{224}Ra due to the rise of pH is obscured by the dramatic increase of ^{224}Ra caused by the rise in salinity, which indicates that the controlling factor of ^{224}Ra in this study is salinity. ORP in the USP shows a negative correlation with ^{224}Ra (Figure 11c). This is because the geochemical reactions in the USP tend to make saline water more reducing (Liu et al., 2017a). Meanwhile, higher salinity of groundwater in the USP corresponds to more organic matter in groundwater induced by seawater infiltration and subsequently more intensive biogeochemical reactions as indicated by Liu et al. (2017c). Therefore, ^{224}Ra in the USP increases with salinity but declines with ORP. In the SW, due to limited organic matter input, the biogeochemical reactions that make groundwater reducing are limited. As a result, the decrease of ^{224}Ra with ORP in the SW is not observed (Figure 11c). The aforementioned relationships between ^{224}Ra and redox indicators and the differences in relationships of the USP and SW are also applicable for ^{223}Ra and ^{228}Ra. More details of relationships between ^{223}Ra (^{228}Ra) and redox indicators can be found in supporting information Figure S1 (supporting information Figure S5).
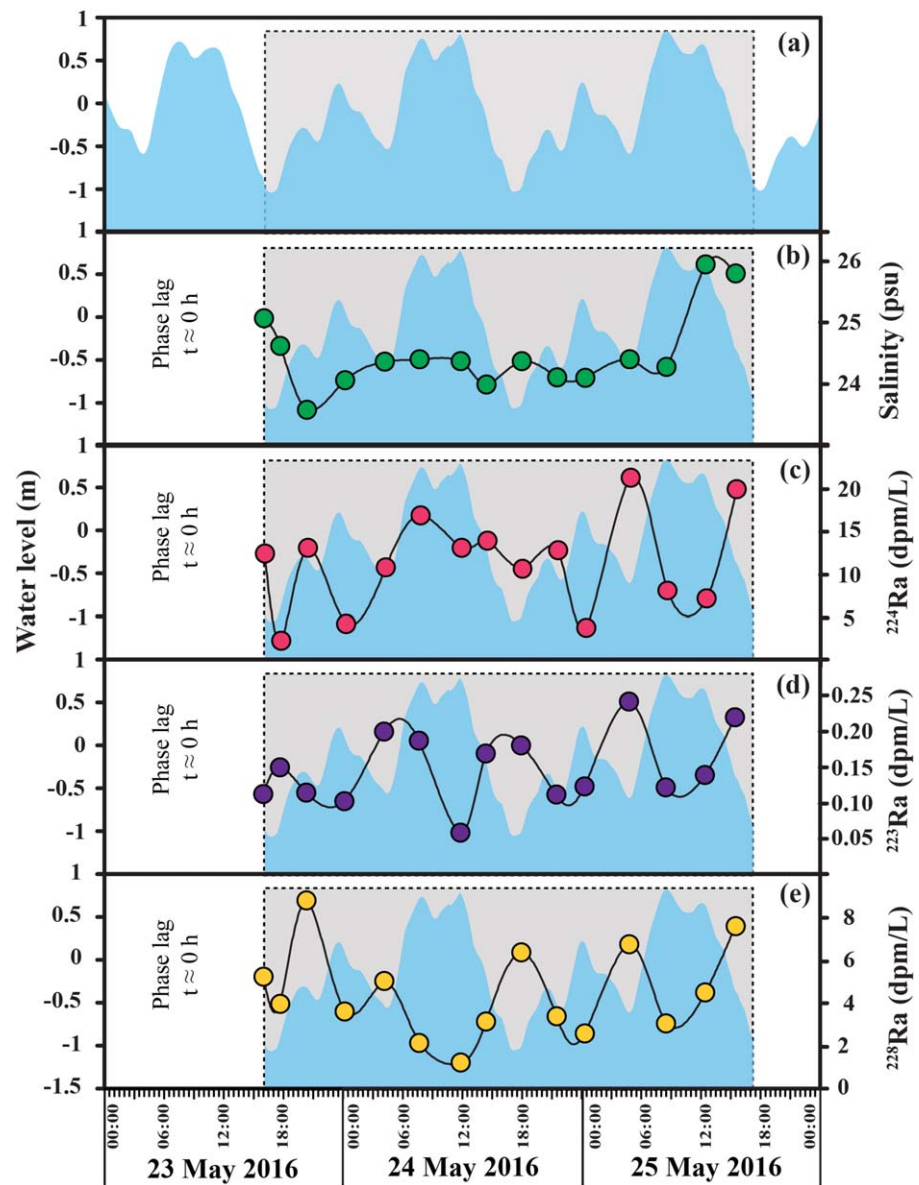
Figure 10. The variations of (a) tidal level, (b) salinity, (c) ^{224}Ra, (d) ^{223}Ra, and (e) ^{228}Ra at nearshore area.

4.3. Using Radium Isotopes to Trace Dissolved Inorganic Carbon Processes in the USP and SW

Total alkalinity is produced via biodegradation of organic matter in groundwater and aquifers. Sulfate reduction-induced remineralization of organic matter, which affects total alkalinity, was also discovered in the study site (Liu et al., 2017b). In addition, nutrient dynamics in the near-surface area presented in Liu et al. (2017c) indicated that biodegradation of organic matter carried by infiltrated seawater produced the majority of total alkalinity along with nutrients such as ammonium (NH_4^+) and phosphate (PO_4^{3-}). A simultaneous increase of total alkalinity and ^{224}Ra (Figure 12a) is observed in both the USP and SW transition zones. Obviously, the production of total alkalinity is much higher in the USP transition zone than in the SW transition zone. This is because infiltrated seawater with comparatively high content of organic matter supports the production of total alkalinity in the USP whereas the organic matter is significantly consumed by geochemical reactions before circulated seawater transport to L3–5 and cannot support a high production of total alkalinity. As a conclusion, the enrichment of total alkalinity in the USP results from biodegradation of organic matter induced by the infiltration of seawater while the slight rise of total alkalinity in the SW is caused by remineralization via sulfate reduction of organic matter that exists in the aquifer. The correlation
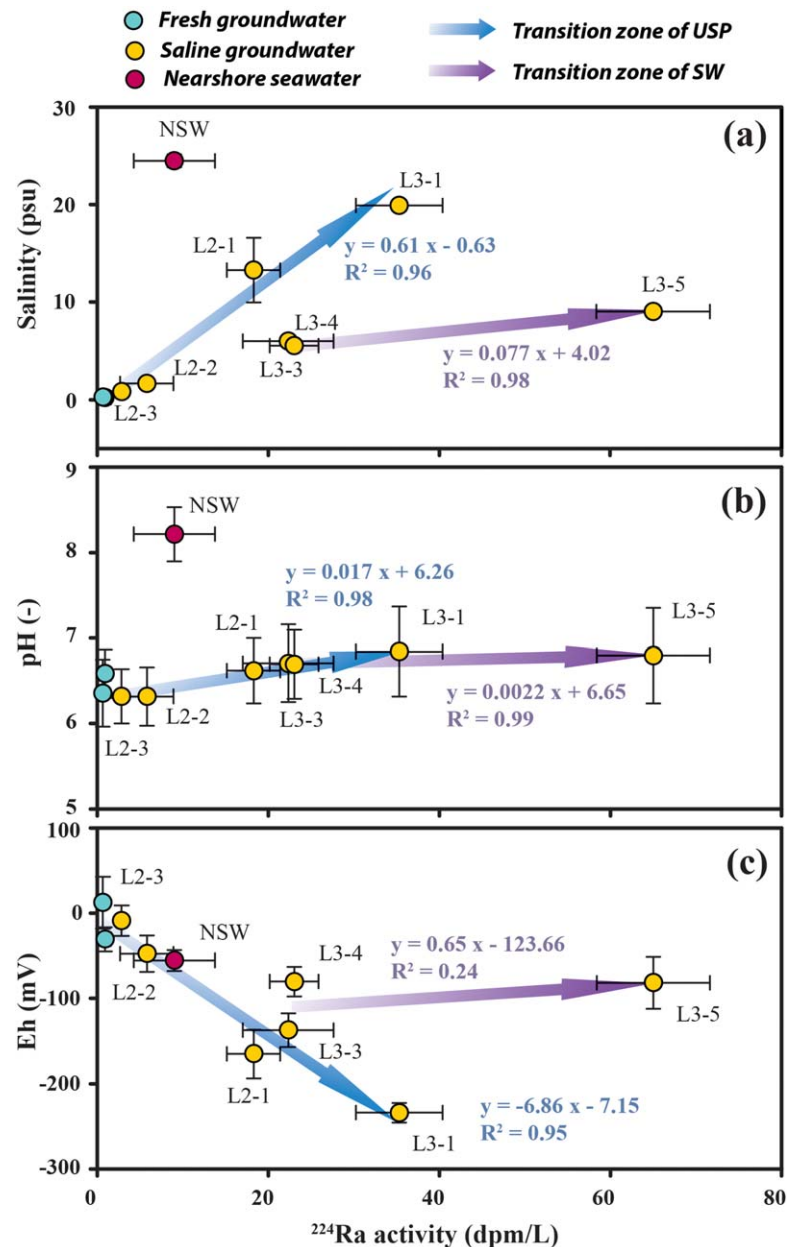
Figure 11. The relationships between redox indicators and ^{224}Ra. (a) Salinity versus ^{224}Ra, (b) pH versus ^{224}Ra, and (c) ORP versus ^{224}Ra in the USP and SW transition zones.

between DIC and ^{224}Ra (Figure 12b) is very similar to the correlation between total alkalinity and ^{224}Ra, which indicates that HCO_3^-, as a main contributor of total alkalinity, is also a main constituent of DIC in the CGMZ of this study. Because pCO$_2$ is negatively correlated to groundwater pH, the correlation between pCO$_2$ and ^{224}Ra (Figure 12c) has a reverse trend compared to the correlation between pH and ^{224}Ra (Figure 11b). As a result, pCO$_2$ declines with the release of ^{224}Ra in the USP transition zone. In the SW transition zone, there is no large variation of pCO$_2$ observed even though ^{224}Ra increases dramatically from L3-3 to L3–5. This is because groundwater pHs at L3-3 (6.74), L3–4 (6.73), and L3–5 (6.69) are similar (Liu et al., 2017a) and pH is not the main controlling factor in this study as stated in previous section. Geochemical reactions inferred from the relationship between ^{224}Ra and TA, DIC, and pCO$_2$ can also be observed via the relationships between ^{223}Ra (^{228}Ra) and total alkalinity, DIC, and pCO$_2$ as shown in supporting information Figure S2 (supporting information Figure S6).
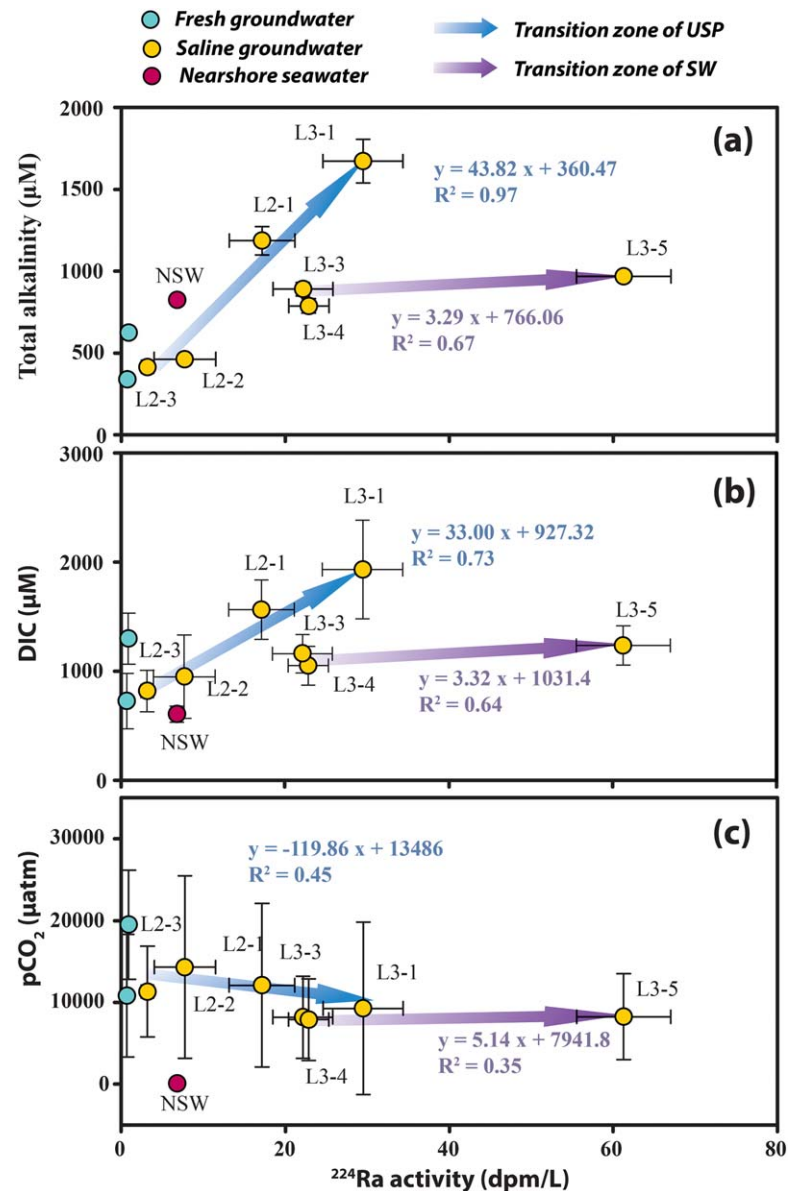
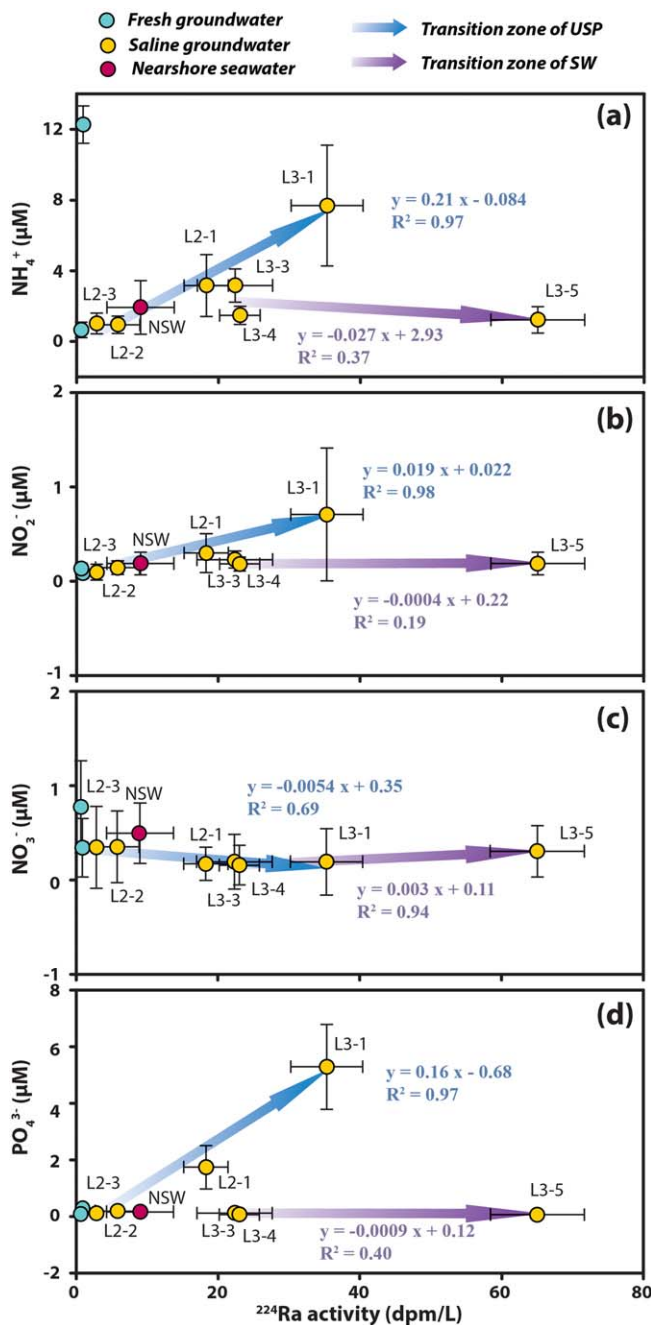**Figure 12.** The relationships between carbon and ^{224}Ra. (a) Total alkalinity versus ^{224}Ra, (b) DIC versus ^{224}Ra, and (c) pCO$_2$ versus ^{224}Ra in the USP and SW transition zones.

4.4. Using Radium Isotopes to Trace Nutrient Processes in the USP and SW

Nutrient dynamics induced by biodegradation of organic matter in the CGMZ are illustrated in Liu et al. (2017c), which indicates that the biodegradation of organic matter in the aquifer is positively correlated to the supply of organic matter with infiltrated seawater. At the same time, infiltration of seawater facilitates the release of ^{224}Ra by enhancing desorption from surface coatings of sediments. Simultaneously, as the products of biodegradation of organic matter, NH_4^+ and PO_4^{3-} increase. This is why concurrent increases of nutrients and ^{224}Ra are observed in the USP transition zone (Figures 13a and 13d). It is worth noting that ^{224}Ra is released by physical desorption of ^{224}Ra from surface coatings of sediments, driven by enhanced ionic strength in high salinity groundwater, rather than from the surfaces of organic matter by biodegradation processes. In the SW transition zone, theoretically, due to the lack of organic matter in this zone, nutrient production would be limited and should produce a uniform concentration of NH_4^+ and PO_4^{3-} in L3-3, L3–4, and L3–5. However, elevated concentrations of NH_4^+ are observed at L3-3 and L3–4 (Figures 13a and 13d), caused by the diffusion of high NH_4^+ in the USP. Even though PO_4^{3-} in the USP is high and will diffuse

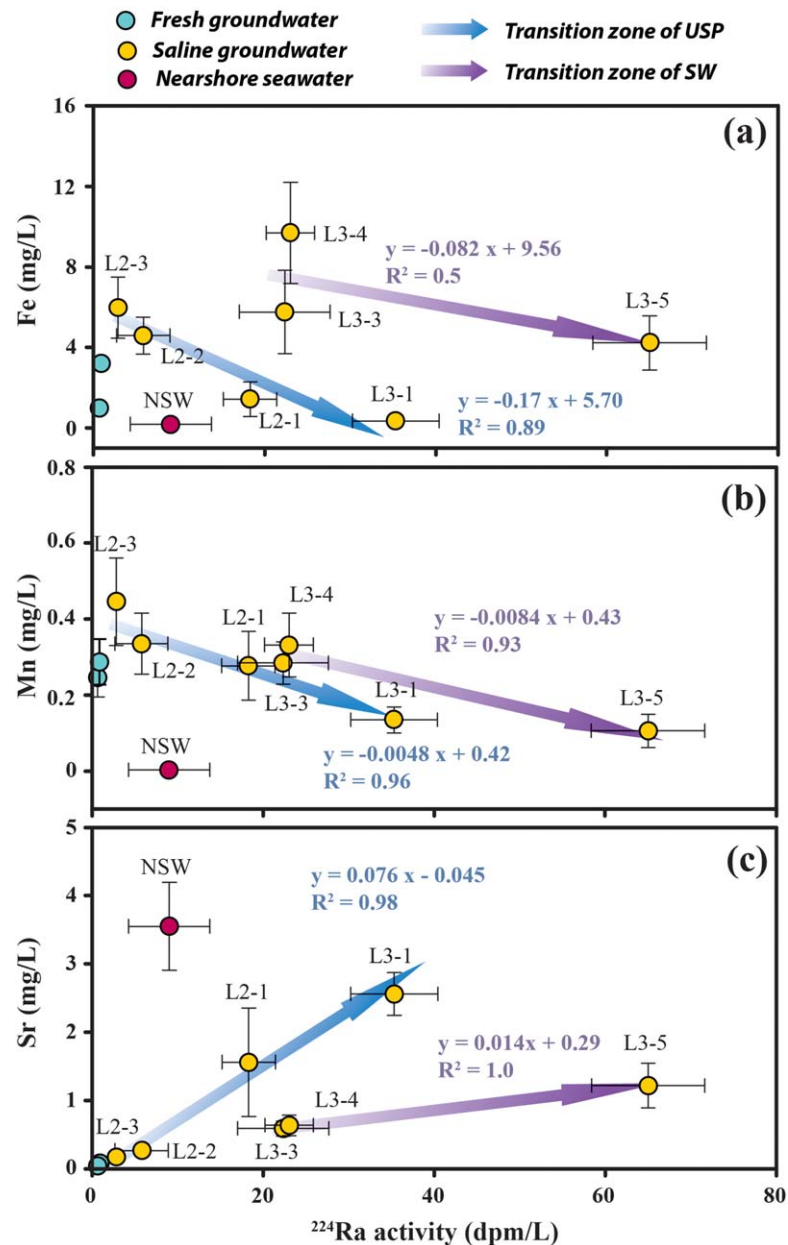**Figure 13.** The relationships between nutrients and ^{224}Ra. (a) NH_4^+ versus ^{224}Ra, (b) NO_2^- versus ^{224}Ra, (c) NO_3^- versus ^{224}Ra, and (d) PO_4^{3-} versus ^{224}Ra in the USP and SW transition zones.

downward, PO_4^{3-} at L3-3 and L3–4 is still very low and shows a different distribution from NH_4^+ (Figure 13d). This is because a large amount of iron oxides exists at L3-3 and because L3–4 adsorbs PO_4^{3-} from groundwater (Liu, 2017). The correlation between NO_2^- and ^{224}Ra in the USP transition zone is identical to the correlation between NH_4^+ and ^{224}Ra in this zone (Figure 13b). This is because NO_2^- is transformed from NH_4^+ via nitrification and the high concentration of NH_4^+ promotes the proceed of nitrification. Consequently, NO_2^- has a positive correlation with ^{224}Ra. The relationship between NO_2^- and ^{224}Ra in the SW transition zone is in accordance with the theoretical situation described previously, under which the production of NO_2^- in the SW is limited and results in a uniform NO_2^- concentration at L3-3, L3–4, and L3–5. NO_3^- shows a very different correlation with ^{224}Ra compared to other nutrients as presented in Figure 13c. The main reason is that the high concentration of NO_3^- is from deep FGW while other nutrients are produced from infiltrated seawater as indicated by Liu et al. (2017c). Therefore, a negative correlation between the NO_3^- and ^{224}Ra is observed in the USP transition zone. In the SW transition zone, the removal of NO_3^- at L3-3 and L3–4 is observed (Figure 13c), which may be caused by denitrification of NO_3^- with the organic matter diffused from the USP. ^{223}Ra and ^{228}Ra have the same implications for nutrients as ^{224}Ra, which are shown in supporting information Figures S3 and S7, respectively. In addition, the differences between nutrient behavior in the USP and SW can also be observed via the relationships between ^{223}Ra (or ^{228}Ra) and nutrients.

4.5. Using Radium Isotopes to Trace Processes of Trace Metals in the USP and SW

As an active zone for geochemical reactions, the USP transition zone was reported to act as a sink for iron due to oxidation of groundwater borne ferrous iron by dissolved oxygen along with infiltrated seawater in the USP (Charette & Sholkovitz, 2002). However, significant reduction of Fe oxides in the CGMZ has been shown in many other studies (Charette & Sholkovitz, 2006; Kiro et al., 2013; Liu, 2017; Roy et al., 2010). There is an abrupt rise of Fe^{2+} at the freshwater front of transition zones in the USP and SW as shown in Figure 14a, which indicates that the production of Fe^{2+} only occurs in this location. This is because NO_3^- from the deep FGW (L2–4) (Liu et al., 2017c) acts as an oxidizer for iron sulfide oxidation and iron sulfide minerals are found to be significantly present in the CGMZ of this study through SEM images (Liu, 2017). Even though Mn^{2+} and Fe^{2+} show a similar increase at the freshwater front of both the USP and SW transition zones (Figures 14a and 14b), the high concentration of Mn^{2+} is transported from high Mn^{2+} groundwater shallower than L1–2 as indicated by Liu (2017), rather than transformed from manganese minerals by geochemical reactions. The dissolved Fe^{2+} and Mn^{2+} suffer from mixing loss only with the subsequent increase of salinity in the transition zone. This can be demonstrated by linear decreases of Fe^{2+} and Mn^{2+} with ^{224}Ra in both the USP and SW transition zones illustrated in Figures 14a and 14b. The very close trend of Mn^{2+} decrease with ^{224}Ra in both the USP and SW transition zones (Figure 14b) suggests that there are no further geochemical reactions involving Mn^{2+} or manganese oxides in the two zones. This is because ^{224}Ra has a strong affinity to manganese oxides (Charette et al., 2005; Charette & Sholkovitz, 2006), and any geochemical reactions of manganese oxides in the aquifer will be detected by the change of ^{224}Ra in groundwater. Sr^{2+} is very conservative in the CGMZ and highly correlated to salinity (Beck et al., 2013; Gonneea et al., 2014; Trezzi et al., 2017), therefore, a simultaneous increase in Sr^{2+} and ^{224}Ra is observed (Figure 14c). Figure 14c indicates that Sr^{2+} has a higher rate of increase with ^{224}Ra in the

Figure 14. The relationships between trace metals and ^{224}Ra. (a) Fe versus ^{224}Ra, (b) Mn versus ^{224}Ra, and (c) Sr versus ^{224}Ra in the USP and SW transition zones.

SW transition zone than in the USP transition zone. Geochemical reactions of trace metals in the CGMZ and differences of trace metal behavior in the USP and SW can also be differentiated from the relationships between ^{223}Ra (or ^{228}Ra) and trace metals, which is shown in supporting information Figure S4 (or in supporting information Figure S8).

5. Conclusions

Since naturally occurring radium isotopes (^{224}Ra, ^{223}Ra, and ^{228}Ra) are powerful tools to trace SGD flux and material transfer across the sediment/water interface, it is of importance to investigate the spatial distribution and temporal variation of radium isotopes in the CGMZ where hydrodynamics, redox conditions, and geochemical reactions are diverse and complex due to the interaction between freshwater and seawater, and various external influencing factors such as tidal fluctuation and seasonal hydrological variation.

Through field investigation and laboratory analysis, this study presents dynamics of ^{224}Ra, ^{223}Ra, and ^{228}Ra within a period of 2 days in the CGMZ under the effect of tidal fluctuation. The partitioning of radium isotopes and the relative ingrowth rates of radium isotopes determine spatial distributions of radium isotopes and result in differences between radium dynamics in the USP and the SW. Through controlling seawater infiltration, tidal fluctuation alters the salinity distribution in the USP, affects the partitioning of radium isotopes in groundwater, and subsequently controls the temporal variation of radium isotopes in the USP. The dynamics of radium isotopes can be used to detect the dilution induced by infiltration of seawater in the USP and also the delayed reaction of groundwater in response to tidal fluctuation in the SW. Thus, the variation of radium isotopes has implications for hydrodynamics in different water patterns of the CGMZ under the effect of external driving forces such as tidal fluctuation, wave-setup, and seasonal hydrologic variation. In addition, because the distribution of radium isotopes can trace the travel and residence time of groundwater in the aquifer and because the degree of mixing with seawater in the USP and SW and the geochemical processes in the CGMZ are time-dependent, radium isotopes are powerful tools to study both groundwater flow dynamics and geochemical reactions such as biodegradation of organic matter that is controlled by the infiltration of seawater driven by tidal fluctuation in the USP.

References

Beck, A. J., Charette, M. A., Cochran, J. K., Gonneea, M. E., & Peucker-Ehrenbrink, B. (2013). Dissolved strontium in the subterranean estuary—Implications for the marine strontium isotope budget. *Geochimica et Cosmochimica Acta*, *117*, 33–52.

Beck, A. J., & Cochran, M. A. (2013). Controls on solid-solution partitioning of radium in saturated marine sands. *Marine Chemistry*, *156*, 38–48.

Beck, A. J., Rapaglia, J. P., Cochran, J. K., & Bokuniewicz, H. J. (2007). Radium mass-balance in Jamaica Bay, NY: Evidence for a substantial flux of submarine groundwater. *Marine Chemistry*, *106*, 419–441.

Cai, P., Shi, X., Hong, Q., Li, Q., Liu, L., Guo, X., et al. (2015). Using ^{224}Ra/^{228}Th disequilibrium to quantify benthic fluxes of dissolved inorganic carbon and nutrients into the Pearl River Estuary. *Geochimica et Cosmochimica Acta*, *170*, 188–203.

Cai, P., Shi, X., Moore, W. S., & Dai, M. (2012). Measurement of ^{224}Ra:^{228}Th disequilibrium in coastal sediments using a delayed coincidence counter. *Marine Chemistry*, *138–139*, 1–6.

Cai, P., Shi, X., Moore, W. S., Peng, S., Wang, G., & Dai, M. (2014). ^{224}Ra:^{228}Th disequilibrium in coastal sediments: Implications for solute transfer across the sediment-water interface. *Geochimica et Cosmochimica Acta*, *125*, 68–84.

Cao, Z. M., Dai, M. H., Zheng, N., Wang, D. L., Li, Q., Zhai, W. D., et al. (2011). Dynamics of the carbonate system in a large continental shelf system under the influence of both a river plume and coastal upwelling. *Journal of Geophysical Research*, *116*, G02010. https://doi.org/10.1029/2010JG001596

Charette, M. A., & Sholkovitz, E. R. (2002). Oxidative precipitation of groundwater-derived ferrous iron in the subterranean estuary of a coastal bay. *Geophysical Research Letters*, *29*(10). https://doi.org/10.1029/2001GL014512

Charette, M. A., & Sholkovitz, E. R. (2006). Trace element cycling in a subterranean estuary: Part 2. Geochemistry of the pore water. *Geochimica et Cosmochimica Acta*, *70*, 811–826.

Charette, M. A., Sholkovitz, E. R., & Hansel, C. M. (2005). Trace element cycling in a subterranean estuary: Part 1. Geochemistry of the permeable sediments. *Geochimica et Cosmochimica Acta*, *69*, 2095–2109.

Fetter, C. W. (2000). *Applied hydrogeology*. Upper Saddle River, NJ: Prentice Hall.

Garcia-Solsona, E., Garcia-Orellana, J., Masqué, P., & Dulaiova, H. (2008). Uncertainties associated with ^{223}Ra and ^{224}Ra measurements in water via a Delayed Coincidence Counter (RaDeCC). *Marine Chemistry*, *109*, 198–219.

Garcia-Solsona, E., Garcia-Orellana, J., Masque, P., Rodellas, V., Mejias, M., Ballesteros, B., et al. (2010). Groundwater and nutrient discharge through karstic coastal springs (Castello, Spain). *Biogeosciences*, *7*, 2625–2638.

Gonneea, M. E., Charette, M. A., Liu, Q., Herrera-Silveira, J. A., & Morales-Ojeda, S. M. (2014). Trace element geochemistry of groundwater in a karst subterranean estuary (Yucatan Peninsula, Mexico). *Geochimica et Cosmochimica Acta*, *132*, 31–49.

Gonneea, M. E., Morris, P. J., Dulaiova, H., & Charette, M. A. (2008). New perspectives on radium behavior within a subterranean estuary. *Marine Chemistry*, *109*, 250–267.

Gonneea, M. E., Mulligan, A. E., & Charette, M. A. (2013). Seasonal cycles in radium and barium within a subterranean estuary: Implications for groundwater derived chemical fluxes to surface waters. *Geochimica et Cosmochimica Acta*, *119*, 164–177.

Hancock, G. J., Webster, I. T., Ford, P. W., & Moore, W. S. (2000). Using Ra isotopes to examine transport processes controlling benthic fluxes into a shallow estuarine lagoon. *Geochimica et Cosmochimica Acta*, *64*, 3685–3699.

Heiss, J. W., & Michael, H. A. (2014). Saltwater-freshwater mixing dynamics in a sandy beach aquifer over tidal, spring-neap, and seasonal cycles. *Water Resources Research*, *50*, 6747–6766. https://doi.org/10.1002/2014WR015574

Hong, Q., Cai, P., Shi, X., Li, Q., & Wang, G. (2017). Solute transport into the Jiulong River estuary via pore water exchange and submarine groundwater discharge: New insights from ^{224}Ra/^{228}Th disequilibrium. *Geochimica et Cosmochimica Acta*, *198*, 338–359.

Kiro, Y., Weinstein, Y., Starinsky, A., & Yechieli, Y. (2013). Groundwater ages and reaction rates during seawater circulation in the Dead Sea aquifer. *Geochimica et Cosmochimica Acta*, *122*, 17–35.

Kiro, Y., Weinstein, Y., Starinsky, A., & Yechieli, Y. (2014). The extent of seawater circulation in the aquifer and its role in elemental mass balances: A lesson from the Dead Sea. *Earth and Planetary Science Letters*, *394*, 146–158.

Kiro, Y., Weinstein, Y., Starinsky, A., & Yechieli, Y. (2015). Application of radon and radium isotopes to groundwater flow dynamics: An example from the Dead Sea. *Chemical Geology*, *411*, 155–171.

Kiro, Y., Yechieli, Y., Voss, C. I., Starinsky, A., & Weinstein, Y. (2012). Modeling radium distribution in coastal aquifers during sea level changes: The Dead Sea case. *Geochimica et Cosmochimica Acta*, *88*, 237–254.

Koulouris, G. (1996). Sorption and distribution of ^{226}Ra in an electrolytic manganese dioxide column in the presence of other ions. *Journal of Radioanalytical and Nuclear Chemistry Letters*, *212*, 131–141.

Krest, J. M., & Harvey, J. W. (2003). Using natural distributions of short-lived radium isotopes to quantify groundwater discharge and recharge. *Limnology and Oceanography: Methods*, *48*, 290–298.

Lee, C. M., Jiao, J. J., Luo, X., & Moore, W. S. (2012). Estimation of submarine groundwater discharge and associated nutrient fluxes in Tolo Harbour, Hong Kong. *Science of the Total Environment*, *433*, 427–433.

Levanon, E., Shalev, E., Yechieli, Y., & Gvirtzman, H. (2016). Fluctuations of fresh-saline water interface and of water table induced by sea tides in unconfined aquifers. *Advances in Water Resources*, *96*, 34–42.

Levanon, E., Yechieli, Y., Gvirtzman, H., & Shalev, E. (2017). Tide-induced fluctuations of salinity and groundwater level in unconfined aquifers—Field measurements and numerical model. *Journal of Hydrology*, *551*, 665–675.

Li, H., Sun, P., Chen, S., Xia, Y., & Liu, S. (2010). A falling-head method for measuring intertidal sediment hydraulic conductivity. *Ground Water*, *48*, 206–211.

Liu, Q., Dai, M., Chen, W., Huh, C. A., Wang, G., Li, Q., et al. (2012). How significant is submarine groundwater discharge and its associated dissolved inorganic carbon in a river-dominated shelf system? *Biogeosciences*, *9*, 1777–1795.

Liu, Y. (2017). *Geochemical processes and solute transport in coastal groundwater mixing zone* (PhD thesis). Hong Kong: The University of Hong Kong.

Liu, Y., Jiao, J. J., & Cheng, H. K. (2018). Tracing submarine groundwater discharge flux in Tolo Harbor, Hong Kong (China). *Hydrogeology Journal*. https://doi.org/10.1007/s10040-018-1736-z

Liu, Y., Jiao, J. J., & Liang, W. (2017a). Tidal fluctuation influenced physicochemical parameter dynamics in coastal groundwater mixing zone. *Estuaries and Coasts*, 1–14. https://doi.org/10.1007/s12237-017-0335-x

Liu, Y., Jiao, J. J., Liang, W., & Kuang, X. (2017b). Hydrochemical characteristics in coastal groundwater mixing zone. *Applied Geochemistry*, *85*, 49–60.

Liu, Y., Jiao, J. J., Liang, W., & Luo, X. (2017c). Tidal pumping induced nutrients dynamics and biogeochemical implications in an intertidal aquifer. *Journal of Geophysical Research: Biogeosciences*, *122*, 3322–3342. https://doi.org/10.1002/2017JG004017

Liu, Y., Jiao, J. J., & Luo, X. (2016). Effects of inland water level oscillation on groundwater dynamics and land-sourced solute transport in a coastal aquifer. *Coastal Engineering*, *114*, 347–360.

Luo, X., Kwok, K. L., Liu, Y., & Jiao, J. (2017). A permanent multilevel monitoring and sampling system in the coastal groundwater mixing zones. *Ground Water*, *55*, 577–587.

Luo, X., & Jiao, J. J. (2016). Submarine groundwater discharge and nutrient loadings in Tolo Harbor, Hong Kong using multiple geotracer-based models, and their implications of red tide outbreaks. *Water Research*, *102*, 11–31.

Luo, X., Jiao, J. J., Moore, W. S., & Lee, C. M. (2014). Submarine groundwater discharge estimation in an urbanized embayment in Hong Kong via short-lived radium isotopes and its implication of nutrient loadings and primary production. *Marine Pollution Bulletin*, *82*, 144–154.

Michael, H. A., Charette, M. A., & Harvey, C. F. (2011). Patterns and variability of groundwater flow and radium activity at the coast: A case study from Waquoit Bay, Massachusetts. *Marine Chemistry*, *127*, 100–114.

Moore, W. S. (2000a). Ages of continental shelf waters determined from Ra-223 and Ra-224. *Journal of Geophysical Research*, *105*, 22117–22122.

Moore, W. S. (2000b). Determining coastal mixing rates using radium isotopes. *Continental Shelf Research*, *20*, 1993–2007.

Moore, W. S. (2008). Fifteen years experience in measuring ^{224}Ra and ^{223}Ra by delayed-coincidence counting. *Marine Chemistry*, *109*, 188–197.

Moore, W. S. (2010). The effect of submarine groundwater discharge on the ocean. *Annual Review of Marine Science*, *2*, 59–88.

Moore, W. S., & Arnold, R. (1996). Measurement of ^{223}Ra and ^{224}Ra in coastal waters using a delayed coincidence counter. *Journal of Geophysical Research*, *101*, 1321–1329.

Moore, W. S., Beck, M., Riedel, T., van der Loeff, M. R., Dellwig, O., Shaw, T. J., et al. (2011). Radium-based pore water fluxes of silica, alkalinity, manganese, DOC, and uranium: A decade of studies in the German Wadden Sea. *Geochimica et Cosmochimica Acta*, *75*, 6535–6555.

Moore, W. S., Blanton, J. O., & Joye, S. B. (2006). Estimates of flushing times, submarine groundwater discharge, and nutrient fluxes to Okatee Estuary, South Carolina. *Journal of Geophysical Research*, *111*, C09006. https://doi.org/10.1029/2005JC003041

Paytan, A., Moore, W. S., & Kastner, M. (1996). Sedimentation rate as determined by ^{226}Ra activity in marine barite. *Geochimica et Cosmochimica Acta*, *60*, 4313–4319.

Porcelli, D. (2008). Chapter 4 investigating groundwater processes using U- and Th-series nuclides. In Krishnaswami, S., & Cochran, J. K. (Eds.), *Radioactivity in the environment* (pp. 105–153). New York, NY: Elsevier.

Robinson, C., Li, L., & Barry, D. A. (2007). Effect of tidal forcing on a subterranean estuary. *Advances in Water Resources*, *30*, 851–865.

Roy, M., Martin, J. B., Cherrier, J., Cable, J. E., & Smith, C. G. (2010). Influence of sea level rise on iron diagenesis in an east Florida subterranean estuary. *Geochimica et Cosmochimica Acta*, *74*, 5560–5573.

Roy, M., Martin, J. B., Smith, C. G., & Cable, J. E. (2011). Reactive-transport modeling of iron diagenesis and associated organic carbon remineralization in a Florida (USA) subterranean estuary. *Earth and Planetary Science Letters*, *304*, 191–201.

Shi, X., Mason, R. P., Charette, M. A., Mazrui, N. M., & Cai, P. (2018). Mercury flux from salt marsh sediments: Insights from a comparison between ^{224}Ra/^{228}Th disequilibrium and core incubation methods. *Geochimica et Cosmochimica Acta*, *222*, 569–583.

Swarzenski, P. W. (2007). U/Th series radionuclides as coastal groundwater tracers. *Chemical Reviews*, *107*, 663–674.

Trezzi, G., Garcia-Orellana, J., Rodellas, V., Masque, P., Garcia-Solsona, E., & Andersson, P. S. (2017). Assessing the role of submarine groundwater discharge as a source of Sr to the Mediterranean Sea. *Geochimica et Cosmochimica Acta*, *200*, 42–54.

Tricca, A., Porcelli, D., & Wasserburg, G. J. (2000). Factors controlling the groundwater transport of U, Th, Ra, and Rn. *Journal of Earth System Science*, *109*, 95–108.

Tricca, A., Wasserburg, G. J., Porcelli, D., & Baskaran, M. (2001). The transport of U- and Th-series nuclides in a sandy unconfined aquifer. *Geochimica et Cosmochimica Acta*, *65*, 1187–1210.

Webster, I. T., Hancock, G. J., & Murray, A. S. (1995). Modeling the effect of salinity on radium desorption from sediments. *Geochimica et Cosmochimica Acta*, *59*, 2469–2476.